國 立 交 通 大 學
光 電 工 程 研 究 所

碩士論文

850nm 面射型雷射之高速特性量測與分析

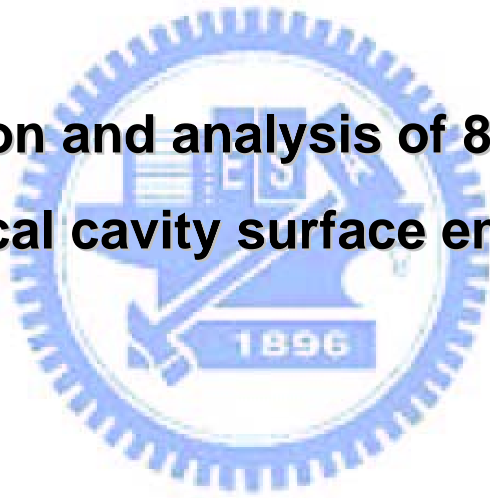

Calculation and analysis of 850nm high speed vertical cavity surface emitting lasers

研究生：呂俊毅

指導教授：王興宗教授

中華民國九十三年六月

850nm 面射型雷射之高速特性量測與分析

Calculation and analysis of 850nm high speed vertical cavity surface emitting lasers

研究生:呂俊毅 Student : Chun-Yi Lu

指導教授:王興宗 教授 Advisor : Shing-Chung Wang

國 立 交 通 大 學

光電工程研究所

碩 士 論 文

A Thesis

Submitted to Institute of Electro-Optical Engineering

College of Electrical Engineering and Computer Science

National Chiao Tung University

in Partial Fulfillment of the Requirements

for the Degree of

Master

In

Electro-Optical Engineering

June 2004

Hsinchu, Taiwan, Republic of China

中華民國 九十三 年 六 月

850nm 面射型雷射之高速特性量測與分析

研究生:呂俊毅　　　　　　　　　　　指導教授:王興宗 教授

交通大學光電工程研究所

摘要

本論文針對砷化鎵(GaAs)之面射型雷射(VCSEL)，在進行離子佈植製程後，對於氧化型面射型雷射高速特性影響進行研究分析，並逐一建立元件結構之等效電路模型來進行模擬比對。研究的 850nm VCSEL，其磊晶結構為上及下反射層分別由 22 及 32 層$Al_{0.15}Ga_{0.85}As$ / $Al_{0.9}Ga_{0.1}As$構成，主動層為GaAs / AlGaAs多重量子井，氧化層$Al_{0.98}Ga_{0.02}As$成長於主動層上三層處。在高速特性量測方面，完成建立一晶圓級之量測系統，可在製程之後直接點測元件的高速特性，以避免封裝對於元件造成調變速度限制。

由於離子佈植為簡易且有效降低元件寄生電容的方式，本論文以普遍製作高速元件之氧化型VCSEL做一比較實驗。實驗量測結果顯示，在同樣氧化孔徑 8μm 下，只有氧化結構之VCSEL與經過離子佈植製程後之VCSEL，其調變速度分別為 2.3 及 8.4 GHz。接著在相同離子佈植條件下，改變氧化孔徑大小為 6、7、8μm，量測得其調變電流效率係數(MCEF)分別為 3.06、5.54 及 5.96 GHz /$mA^{1/2}$。

接著根據不同的 VCSEL 結構，建立一等效電路模型，以 Agilent ADS 程式進行模擬(modeling)，分析元件結構等效 RC 電路對高速調變的影響。由等效電路的分析模擬，可以更清楚瞭解元件結構影響高速特性的程度，進而改進元件製程，以期能製造出更高速的 VCSEL。

Calculation and analysis of 850nm high speed vertical cavity surface emitting lasers

Student: Chun-Yi Lu　　　　　　Advisors: Dr. Shing-Chung Wang

Institute of Electro-Optical Engineering
National Chiao Tung University

Abstract

This research is focusing on the study of high speed modulation characteristics of GaAs base vertical cavity surface emitting laser (VCSEL) with oxide-confined and oxide-implant structure, and establishes an equivalent circuit model for electrical characteristic analysis. The 850nm VCSEL structure consists of GaAs /AlGaAs multi-quantum-well. Top and bottom distributed bragg reflector has 22 and 32 pairs $Al_{0.15}Ga_{0.85}As$ /$Al_{0.9}Ga_{0.1}As$ respectively. We setup an on-wafer high speed measurement system which benefits us to test device immediately and avoid modulation limitation from package.

Proton implant process is a simple method to reduce parasitic capacitance. For this, we fabricate oxide-only and oxide-implant VCSEL and compare with their modulation characteristics. With same oxide aperture size 8μm, oxide-implant VCSEL has better modulation bandwidth 8.4 GHz and oxide-only VCSEL has 2.3 GHz. Then we compare oxide-implant VCSEL with different oxide aperture size as 6, 7 and 8μm, and obtain modulation current efficiency factor (MCEF) as 3.06, 5.54 and 5.96 GHz /$mA^{1/2}$ respectively.

We build an equivalent circuit model, corresponding different VCSEL structure, for modeling the modulation limitation, affected by RC circuit, and simulate circuit by Agilent Advanced Design System software. The simulation results could make the modulation limitation clearly and help us to modify the VCSEL process for high speed operation.

致謝

在交通大學光電工程研究所求學研究的這兩年，不僅在學問上獲得不少收穫，在人與人之間的互動上，亦學習到如何平和的相處與溝通。

首先，感謝指導老師王興宗教授，讓我有機會進入本實驗室學習，最重要的是讓我清楚瞭解到做研究應有態度及方法，另外也非常感謝王老師對於研究實驗上的全力支持。感謝郭浩中教授在實驗上的指導，使得整個論文研究過程，很順利的完成。

在此要特別感謝張亞銜學長，在過去一年半的時間裡，從實驗的建立，一直到完成研究這過程的指導及協助，並一起解決實驗上所遇到的各種問題。另外，也非常感謝道鴻學長在論文撰寫上的指教，芳儀學姐及聖彬學長在儀器操作上的指導，以及賴利弘學長和林佳鋒學長在研究方面的建議指教。感謝羅俊麟同學在學問上的切磋與討論，使我更清楚釐清實驗的原理。感謝張鴻儒學長熱心的分享人生經驗，使我獲益良多。

感謝老余、老朱、忻宏、小朱、聖彬、哲偉、峻瑋學長們及文君學姐，在我們剛進實驗室時，多方面的扶持與協助，也非常懷念去年學長姐忙於畢業而我們同學都忙於實驗那段時光，對於某種娛樂的執著與其技藝上切磋，雖然這不是研究實驗的一部份，但這也使得我們的相處更加融洽。非常感謝同學們，志強、永龍、妙佳、威佑與偉倫，在過去這些日子彼此互相勉勵與扶持，以及學業上的指教與討論；另外一同出遊的愉快經驗，讓我的研究生生活更增添許多愉快回憶，真的非常感謝你們。還有碩一的學弟妹國峰、文燈、薏婷、裕鈞、敏瑛、永昌、瑞溢及傳煜，謝謝你們的幫忙，跟你們相處非常的愉快。

最後，衷心的感謝我的父母與哥哥，在這段日子來的支持，讓我能夠順利完成學業，非常感謝你們！

Contents

List of Tables……………………………………………………………………...V

List of Figures…………………………………………………………………..….VI

Chapter 1 Introduction and overview……………………………………………...1

1-1 Review of VCSEL……………………………………………………1

1-2 Fundamental of VCSEL……………………………………………...2

1-3 Development trend……..……………………………………………4

Chapter 2 Theorem of modulating VCSEL………………………………………11

2-1 Recombination mechanism of VCSEL……………………………12

2-2 Transfer function……………………………………………………15

2-3 Scattering parameters………………………………………………19

2-4 Summary……………………………………………………………21

Chapter 3 VCSEL design and measurement setup………………………………28

3-1 Fabrication of oxide-confined VCSEL………………………………28

3-2 Fabrication of oxide-implant VCSEL…………………………………29

3-3 Probe station and spectrum measurement system………………...30

3-4 Microwave test system………………………………………………31

Chapter 4 High speed measurement and modeling analysis……………………41

4-1 Comparison oxide-confined and oxide-implant VCSEL……………42

4-2 Comparison oxide-implant VCSELs in different oxide aperture sizes…..…………………………………………………………43

4-3 Equivalent circuit design and modeling……………………………44

Chapter 5 Conclusion………………………………………………………………57

Reference……………………………………………………………………………58

List of Tables

Table 1-1 History of VCSEL research……………………………………………10

Table 4-1 Equivalent circuit elements at different bias current for

oxide-only VCSEL…………………………………………………56

Table 4-2 Equivalent circuit elements at different bias current for

oxide-implant VCSEL………………………………………………56

List of Figures

Figure 1-1 A modal of vertical cavity surface emitting laser (VCSEL)……………6

Figure 1-2 Material for VCSELs in wide spectral bands……………………………6

Figure 1-3 Structure for current confinement for VCSELs…………………………7

Figure 1-4 Global consumption value of diode laser by the year 2002…………....8

Figure 1-5 Global consumption value of diode by the year 2002
(distinguished into wavelength)..8

Figure 1-6 Transmission spectrum for silica fiber…………………………………9

Figure 2-1 Band diagram of active region of VCSEL……………………………..22

Figure 2-2 Reservoir analogy (a) under threshold (b) above threshold…………23

Figure 2-3 Basic electronic recombination/generation mechanism……………..24

Figure 2-4 Schematic of VCSEL illustrating active region and cavity volumes
……………………………………………………………………………25

Figure 2-5 Conversion from electrical small signal train into optical signal…….25

Figure 2-6 Small signal modulation response of a VCSEL………………………26

Figure 2-7 Common terms for high-frequency device characterization…………26

Figure 2-8 A simple two-port network is defined as S-parameters………………27

Figure 3-1 Cross section structure of ring-trenched VCSEL structure…………..33

Figure 3-2 Steps of oxide-confined VCSEL process……………………………...34

Figure 3-3 Illustration of oxidation process system setup………………………..35

Figure 3-4 Oxidation rate of 98% Al-content layer………………………………...35

Figure 3-5 OM-image of VCSEL with 6μm oxide-aperture……………………….36

Figure 3-6 Steps of oxide-implant VCSEL process……………………………….37

Figure 3-7 Proton-implant depth with different energy simulating by Trim……..38

Figure 3-8 Probe station measurement instrument setup………………………..39

Figure 3-9 Microwave test system set-up……………………………………….39

Figure 3-10 Sub-mount substrate design……………………………………….40

Figure 3-11 Illustration of microwave test system……………………………….40

Figure 4-1 Oxide-only and oxide-implant VCSEL structure………………………46

Figure 4-2 Typical LIV curve for oxide-only and oxide-implant VCSELs………47

Figure 4-3 Modulation responses for both oxide-only and oxide-implant VCSELs

…………………………………………………………………………48

Figure 4-4 Resonance and 3dB frequency as a function of $(I-I_{th})^{1/2}$ for

oxide-only and oxide-implant VCSELs………………………………49

Figure 4-5 Eye-diagram for oxide-only and oxide-implant VCSELs…………….50

Figure 4-6 Typical LIV curve for VCSELs with different oxide aperture size

as 6, 7, and 8 μm………………………………………………………51

Figure 4-7 Modulation response of VCSELs with difference oxide aperture

as 6, 7, and 8 μm……………………………………………………..52

Figure 4-8 Resonance and 3dB frequency as a function of $(I-I_{th})^{1/2}$ for

difference oxide aperture VCSELs……………………………………53

Figure 4-9 Real and imaginary S11 parameter versus frequency from model and

measured data…………………………………………………………..54

Figure 4-10 Compared capacitances of oxide-only and oxide-implant

VCSELs…………………………………………………………………55

Chapter 1

Introduction and overview

1-1 Review of VCSEL

Vertical cavity surface emitting lasers (VCSELs) was first demonstrated in 1979 by H. Soda, K. Iga, F. Koyama and S. Kinoshita [1]. While the cavity design was novel as compared to the established edge-emitting lasers, the initial device performance was poor in terms of the high threshold current density and low output power that it apparently attracted little attention. Continued work by Iga and various coworkers, however, showed continuous improvements in performance, eventually leading to the first continuous wave VCSEL operation, at room temperature, reported in 1988 [2]. By that time other important innovations and demonstrations had brought growing attention to the VCSEL. We could look at the brief history of VCSEL research as tabulated in Table 1-1 [3].

The VCSEL structure may provide a number of advantages over traditional lasers, as follow:

- ▲ Low threshold operation for its small cavity volume
- ▲ High-speed modulation capability
- ▲ Low power consumption
- ▲ Low cost chip production
- ▲ Vertical emission from the substrate
- ▲ Easy coupling to optical fiber due to circular beam

- ▲ The initial probe test can be performed before separating device into discrete chips
- ▲ Densely packed and precisely arranged two-dimensional laser arrays
- ▲ Higher reliability
- ▲ Higher integration

The progress of the vertical cavity surface emitting laser in the late 1990s was very fast, and various applications to optoelectronics [4]. In 1992, VCSELs based on GaAs have been extensively studied some of the 0.98, 0.85 and 0.78 μm wavelength devices are now commercialized into optical system. VCSELs are currently to be the ideal laser source for fiber optic application.

1-2 Fundamental of VCSEL

The structure common to most VCSELs consists of two parallel reflectors which sandwich a thin active layer, is illustrated with Figure 1-1. The reflectivity necessary to reach the lasing threshold should normally be higher than 99.9%. Together with the optical cavity formation, the scheme for injecting electrons and holes effectively into the small volume of the active region is necessary for a current injection device. The ultimate threshold current depends on how to make the active volume small and how well the optical field can be confined in the cavity to maximize the overlap with the active region. These confinement structures will be presented later.

There are some choices of the materials for semiconductor lasers in Figure 1-2. The availability of substrates against lattice constant related to the systems

is also shown. The problems are listed below that should be taken into account consideration for making VCSELs:

- ▲ Design of resonant cavity and mode-gain matching
- ▲ Multi-layered distributed Bragg reflectors (DBRs) to realize high-reflective mirrors
- ▲ Heat sinking for high temperature and high power operation

In addition, the resistivity of material is crucial for high speed operation.

These are typical methods of current confinement schemes for the VCSEL structures, indicated in Figure 1-3, reported so far.

- ▲ Ring electrode type: This structure can limit the current flow in the vicinity of the ring electrode. The light output can be taken out from the center window. This is easy to fabricate, but the current can not completely be confined to a small area due to diffusion.
- ▲ Proton-implant type: An insulating layer made by proton (H^+) irradiation to limit the current spreading toward the surrounding area. The progress is rather simple and most commercialized devices are made by this method.
- ▲ Regrowth Buried-Heterostructure (BH) type: The mesa etching including active region form a wide-gap semiconductor to limit the current. The refractive index can be small in the surrounding region, resulting in forming an index-guiding structure. This is one of ideal structures in terms of current and optical confinement. The problem is that the necessary process is rather complicated.
- ▲ Air-post type: The circular or rectangular air post is used to achieve a current confinement. It is the simplest method of device fabrication, but

non-radiative recombination at the outer wall may reduce the performance.

▲ Selective AlAs oxidation type: By oxidizing the AlAs layer to form an insulator.

By developing new process technology could achieve the better laser performance.

1-3 Development trend

The market forecast of 2002 global laser diode market analysis [5], indicated in Figure 1-4, appears that optical communication and storage have almost 84% market demand. Moreover, the market distinguished into wavelength, Figure 1-5, shows 780~980nm laser diode in chief. For telecommunication, development of Ethernet causes the needs of capacity increasing rapidly. Metro-area network (MAN) would use fiber optical communication replace traditional cable to satisfy high-capacity requirement. Local-area network (LAN) would expand fiber to the home (FTTH) which developed rapidly in Japan now. Primary transmission rate is developed almost up to 10Gbps suitable for OC-192 standard by ANSI [6]. Storage-area network (SAN), another major grownth sector, perhaps is the brightest spot in networking. These interconnections link large disk arrays to servers and other systems. The reigning technology is Fiber Channel (FC), an optical ring configuration that has become the standard. FC continues to get faster as the newer versions of the standard have increased rates to 1.0625 Mbits/s and 2.125 Gbits/s, making this system even more desirable today. Faster 4G and 10G systems are in the works.

VCSEL with advantage of wide-band and small-volume transmission capability is an appropriate laser source for those applications. Long wavelength VCSELs provide ultimate transmission capacity in long-distance; 850nm VCSELs are suited to short-distance communication such as LAN. VCSELs contain primary fiber optic communication channels, that is, 850/1310/1550nm which has less attenuation in fiber link, indicated in Figure 1-6. Beside of communication, the high-speed demand for optical storage is growth. International associate precisely define 650nm laser as beam recorder. VCSELs almost contain wide-band transmission application.

The mainstream of commercial high-speed VCSEL is 2.5Gbps (OC-48) and few laboratories and corporations research in 10Gbps device. In this paper, we focus on high-speed 850nm vertical cavity surface emitting lasers. First, we mention major VCSEL structure process, oxide and oxide-implantation, and explain high-speed test system in detail in chapter 2. In chapter 3, a simple introduction of phenomenon approach the rate equation is presented. The scattering coefficients are estimated by high-speed measurement, Transfer function is used in analyzing dynamic characteristics as relaxation frequency, damping rate. We measure static and dynamic characteristics of VCSELs and create an equivalent circuit for modeling in chapter 4. Finally, we give a brief conclusion in chapter 5.

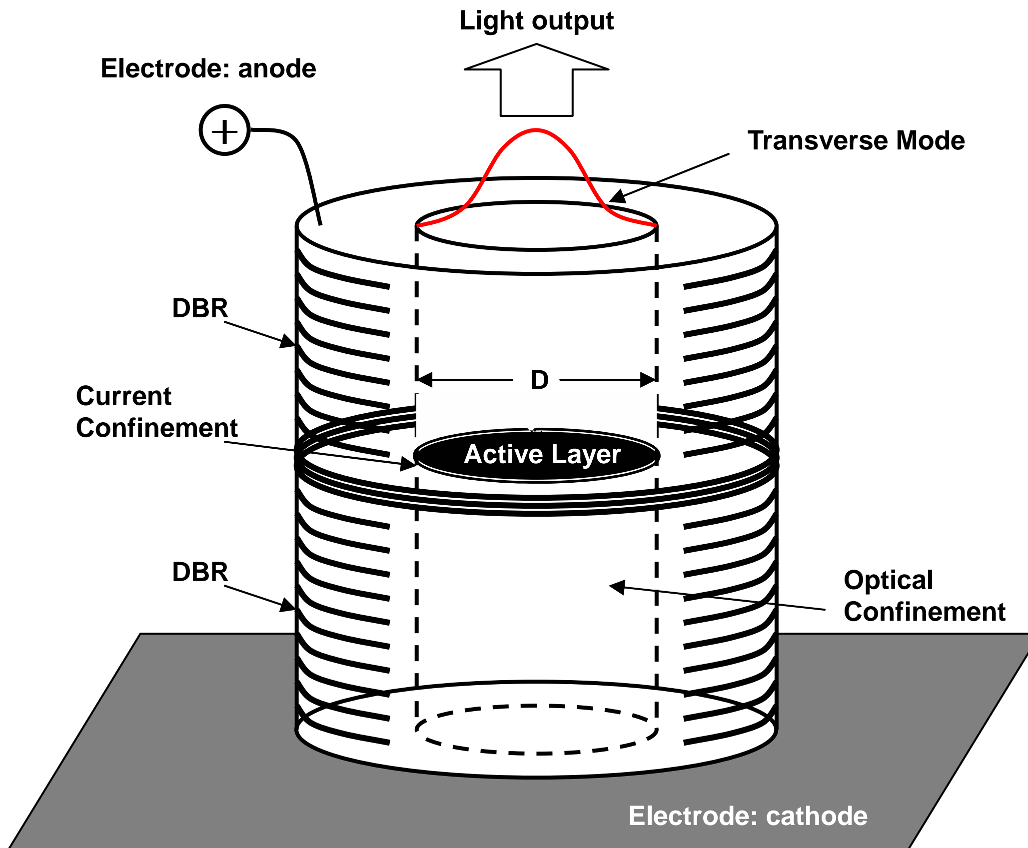

Figure 1-1 A modal of vertical cavity surface emitting laser (VCSEL)

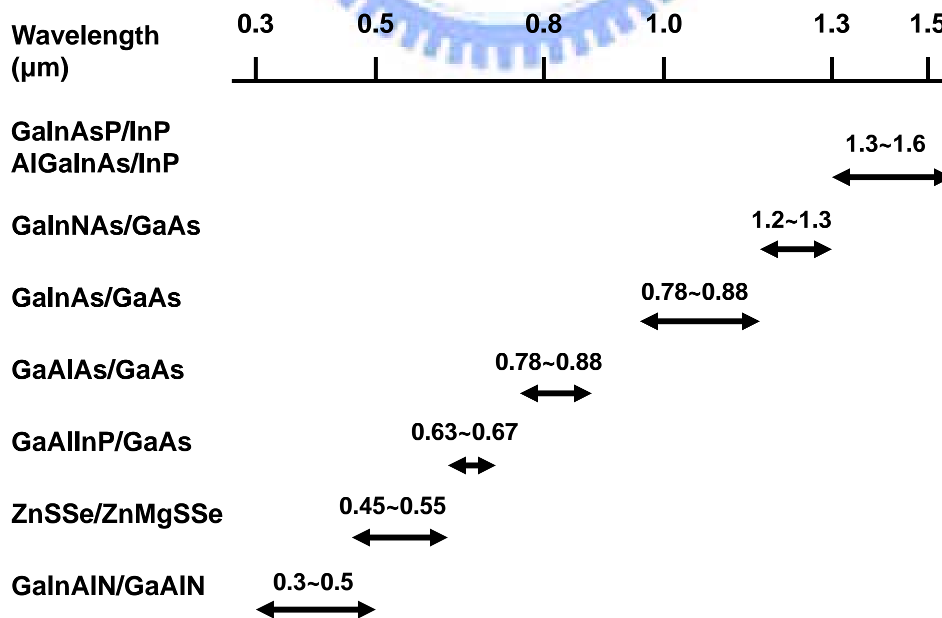

Figure 1-2 Material for VCSELs in wide spectral bands

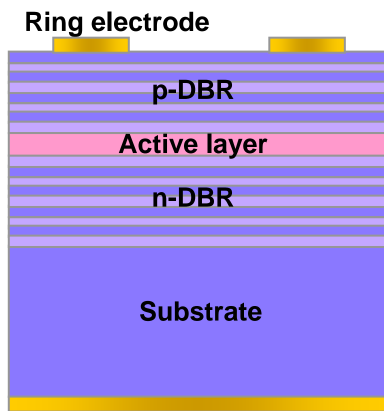

(a) Ring-electrode type

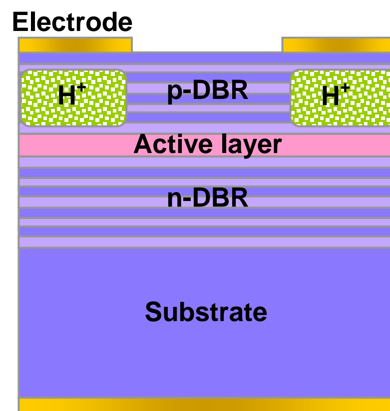

(b) Proton-implant type

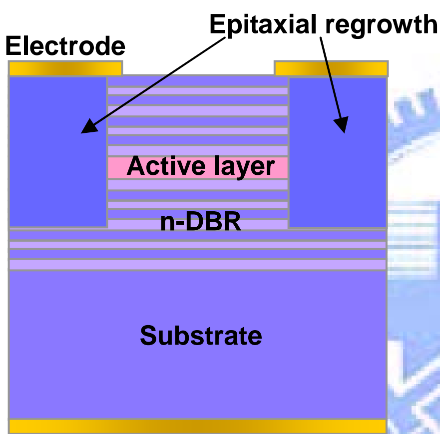

(c) Regrowth BH type

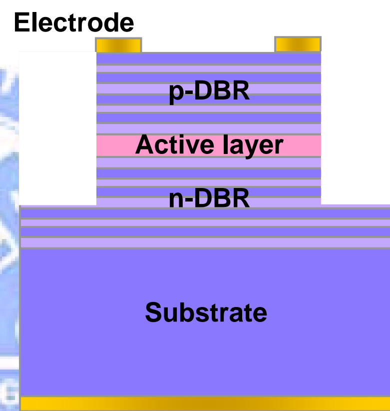

(d) Air-post type

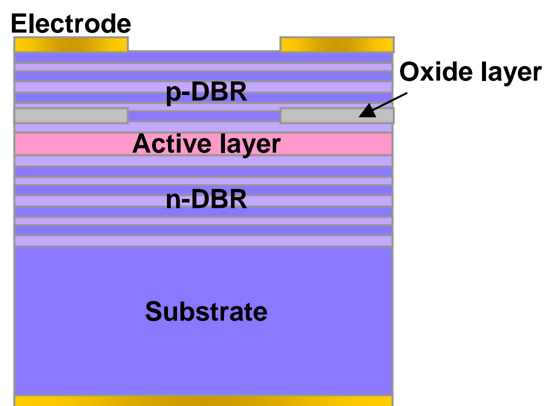

(e) Selective oxidation type

Figure 1-3 Structure for current confinement for VCSELs

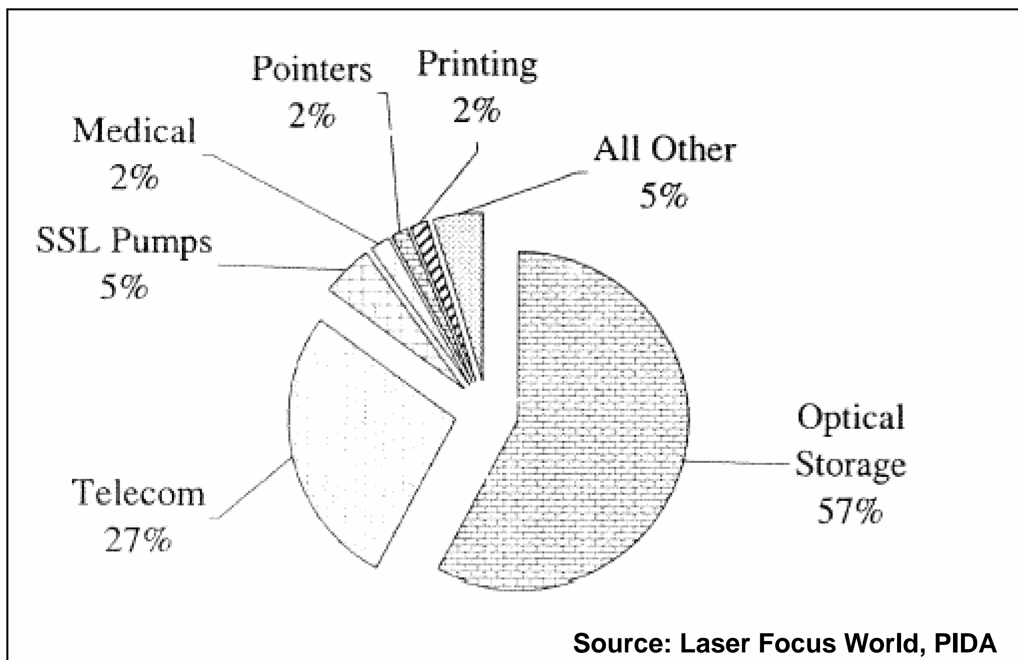

Figure 1-4 Global consumption value of diode laser by the year 2002

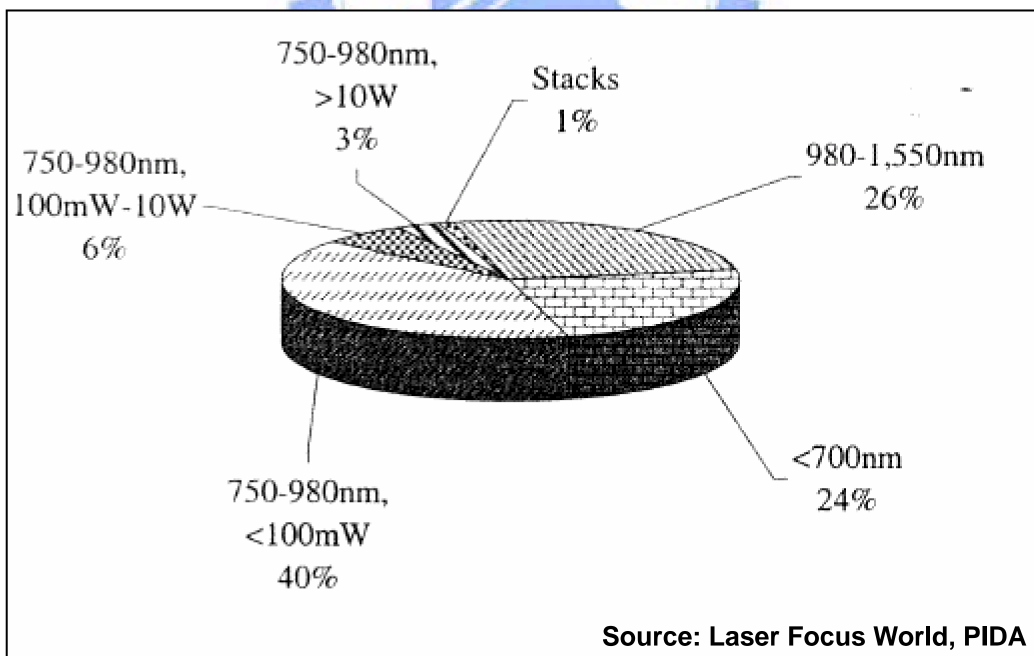

Figure 1-5 Global consumption value of diode by the year 2002
(distinguished into wavelength)

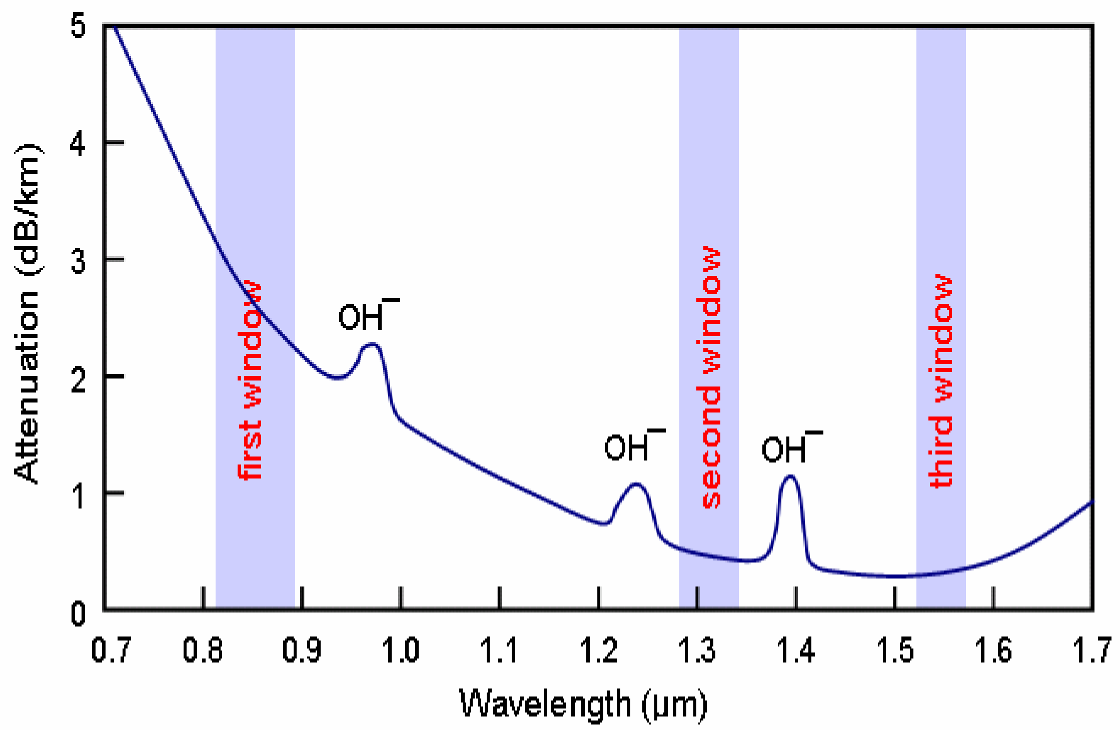

Figure 1-6 Transmission spectrum for silica fiber

Year	Event	Material	Wavelength
1977	First suggestion	GaAlAs/GaAs	0.85 μm
1979	First demonstration	GaInAsP/InP	1.3 μm
1984	Semiconductor DBR	GaInAsP/InP	1.3 μm
1986		GaAlAs/GaAs	0.85 μm
1986	6mA threshold at room temperature	GaAlAs/GaAs	0.85 μm
1988	First room temperature CW	GaAlAs/GaAs	0.85 μm
1989	2mA threshold quantum well device	GaInAs/GaAs	0.98 μm
1989	Sub-mA threshold device	GaInAs/GaAs	0.98 μm
1991	First room temperature operation of deep red	GaAlAs/GaAs	0.78 μm
1993	First room temperature CW long wavelength	GaInAsP/InP	1.3 μm
1993	First room temperature operation of red color	GaInAlP/GaAs	0.67 μm
1995	Oxidation of AlAs and sub-200μA I_{th}	GaInAs/GaAs	0.98 μm
1996	107 hours of lifetime	GaAlAs/GaAs	0.85 μm
1996	> 200mW CW output	GaInAs/GaAs	0.98 μm
1996	> 50% power conversion efficiency	GaInAs/GaAs	0.98 μm
		GaAlAs/GaAs	0.85 μm
1998	Optically pumped blue color	GaInN/GaN	0.4 μm

Table 1-1 History of VCSEL research

Chapter 2

Theorem of VCSEL modulation

The chapter begins by developing a reservoir model for a flow of charge into double-heterostructure active regions and its subsequent recombination. Recombination mechanism is determined by electron-hole recombination at quantum well generates photons for light emission. For this we describe the phenomenological approach to VCSEL first.

The rate equations provide the most fundamental description of the laser in next section. It describes the time-evolution of carrier and photon densities in a laser cavity as a function of the pump rate, material gain and parameters associated with the material properties and laser construction. Dynamic characteristics of VCSEL are studied as rate equation, and it is produced for modulated current injection. Transfer function is relevant equation originated from rate equation which is explained next.

The last section is presented of scattering parameter used in RF measurement. Under small-signal modulation, the rate equations for carriers and photons are found to be analogous to differential equations that describe the current and voltage in an RLC circuit. Scattering parameter offers not only response as bandwidth but reflection coefficient which mirrored equivalent RLC circuit. Establishment of equivalent circuit is purposed to be found the limitation of bandwidth for VCSEL structure and making terminal impedance matching easily.

2-1 Recombination mechanism of VCSEL

The proposition considers the current injected into VCSEL, and suggests it is desirable to have all of it contributes to electrons and holes which recombine in the active region. Since the definitions of the active region and the internal quantum efficiency, η_i, are so critical to further analysis. Active region, evolved into lowest band-gap region, is where recombining carriers contribute to photon emission. Band diagram of active region, includes separate confinement hetero-structure (SCH) band-gap region, illustrated in Figure 2-1. Internal quantum efficiency, η_i, is the fraction of terminal current that generates carriers in the active region. It is important to realize that includes all of the carriers that are injected into active region, not just carriers that recombine induce radiating at the desired transition energy.

The carrier density, n, in the active region is governed by a dynamic process. In fact, we could compare the process of a certain steady-state carrier density in the active region to that a reservoir analogy, which is being simultaneously filled and drained, in a certain water level. This is shown schematically in Figure 2-2(a). For the double heterostructure active region, the injected current provides a generation term and various radiative and nonradiative recombination processes as well as carrier leakage provides recombination term. Thus, rate equation is determined as

$$\frac{dn}{dt} = G_{gen} - R_{rec} \tag{2-1}$$

where G_{gen} is the rate of injected electrons and R_{rec} is the rate of recombining electrons per unit volume in the active region. There are $\eta_i\, I/q$ electrons per

second being injected into the active region. V is the volume of the active region.

The recombination process is accompanied with spontaneous emission rate, R_{sp}, and a nonradiative recombination rate, R_{nr}, depicted in Figure 2-3. Carrier leakage rate, R_l, must be occurred at the transverse and/or lateral potential barrier are not sufficiently high. A net stimulated combination, R_{st}, is including both stimulated absorption and emission. That is, an increased injection results in an increased output, R_{st}, but no increase in carrier density as water level illustrated in Figure 2-2(b). Total recombination rate is expressed as below

$$R_{rec} = R_{sp} + R_{nr} + R_l + R_{st} \tag{2-2}$$

where the first three terms on the right refer to the natural carrier decay processes. It is common to describe the natural decay processes by a carrier lifetime, τ. In the absence of photon generation term, the rate equation for carrier decay is, $dn/dt = n/\tau$, where $n/\tau = R_{sp} + R_{nr} + R_l$, by comparison to Eq. (2-2). Thus, the carrier rate equation in equivalent be expressed as

$$\frac{dn}{dt} = \frac{\eta_i I}{qV} - \frac{n}{\tau} - R_{st} \tag{2-3}$$

The net stimulated recombination rate, R_{st}, in generating photons as well as effect of the resonant cavity in storing photons is investigated additionally. A rate equation for the photon density, n_p, which includes the photon generation and loss terms are constructed analogous to carrier rate equation. The main photon generation term above threshold is R_{st}. Every time an electron-hole pair is stimulated to recombine, another photon is generated. However, as indicated in Figure 2-4, the cavity volume occupied by photons, V_p, is usually larger than the

active region volume occupied by electrons, V, the photon density generation rate will be $(V/V_p)R_{st}$ not just R_{st}. This electron-photon overlap factor, (V/V_p), is generally referred to as the confinement factor, Γ.

Photon loss occurs within the cavity due to optical absorption and scattering out of the mode, and it also occurs at the output coupling mirror where a portion of the resonant mode is usefully coupled to some output medium. These losses could characterize by a photon lifetime, τ_p. The photon rate equation takes the form

$$\frac{dn_p}{dt} = \Gamma R_{st} + \Gamma \beta R_{sp} - \frac{n_p}{\tau_p} \quad (2\text{-}4)$$

where β is the spontaneous emission factor. For uniform coupling to all modes, β is just the number of spontaneous emission coupled into specific mode in the bandwidth of all spontaneous emission.

R_{st} represents the photon stimulated net electron-hole recombination which generates more photons. This is a gain process for photon. An increased photon is proportional to an increased injection carriers overfill the reservoir, which is critical condition to generate stimulated emission, shown in Figure 2-3. The proportion is defined as gain coefficient, $g(n)$. That is,

$$g(n) = g_0(n - n_{tr}) = v_g a(n - n_{tr}) \quad (2\text{-}5)$$

Where a is the differential gain. The term of $a(n - n_{tr})$ is determined approximately to laser oscillation condition with regenerated amplifier approach due to multiple reflection. n_{tr} is a transparency carrier density, and v_g is the group velocity of the mode of interest including both material and waveguide

dispersion. v_g still can be expressed as C/n_r, where C is 3x10^8 m/s and n_r is index of cavity medium. Thus R_{st} is replaced with $g(n)n_p$, and now the carrier and photon density rate equations can be written as

$$\frac{dn}{dt} = \frac{\eta_i I}{qV} - \frac{n}{\tau} - g(n)n_p \qquad (2\text{-}6)$$

$$\frac{dn_p}{dt} = \Gamma g(n)n_p + \Gamma \beta R_{sp} - \frac{n_p}{\tau_p} \qquad (2\text{-}7)$$

Equations (2-6) and (2-7) are two coupled equations that can be solved for the steady-state and dynamic responses of a diode laser in next section.

2-2 Transfer function

Under small signal modulation, the carrier and photon density rate equation, Eq. (2-6) and (2-7), are used to calculate relaxation resonance frequency and its relationship to laser modulation bandwidth.

Consider the application of an above-threshold DC current, I_0, carried with a small AC current, I_m, to a diode laser. Illustration is, shown in Figure 2-5, under basic L-I characteristics (Light output power versus current). The small modulation signal with some possible harmonics of the drive frequency, ω. Small signal approximation, assumes $I_m \ll I_0$ bias and spontaneous emission term, β, is neglected, is expressed as

$$I = I_0 + I_m(t) = I_0 + I_m(\omega)e^{j\omega t}$$

$$n = n_0 + n_m(t) = n_0 + n_m(\omega)e^{j\omega t} \tag{2-8}$$

$$n_p = n_{p0} + n_{pm}(t) = n_{p0} + n_{pm}(\omega)e^{j\omega t}$$

Before applying these to Eq. (2-6) and (2-7), the rate equation is rewritten for the gain. Assumption under DC current is sufficiently above threshold that the spontaneous emission can be neglected. Without loss of generality, we suppose full overlap between the active region and photon field, Γ =1; furthermore, internal quantum efficiency, η_i , is neglected. That is,

$$\frac{dn}{dt} = \frac{I}{qV} - \frac{n}{\tau} - g_0(n - n_{tr})n_p \tag{2-9}$$

$$\frac{dn_p}{dt} = g_0(n - n_{tr})n_p + \beta R_{sp} - \frac{n_p}{\tau_p} \tag{2-10}$$

substitute Eq. (2-8) into Eq. (2-9)

$$\frac{d(n_0 + n_m)}{dt} = \frac{(I_0 + I_m)}{qV} - \left(\frac{n_0 + n_m}{\tau}\right) - g_0(n_0 + n_m - n_{tr})(n_{p0} + n_{pm})$$

$$= \left(\frac{I_0}{qV} - g_0(n_0 - n_{tr})n_{p0} - \frac{n_o}{\tau}\right) + \left(\frac{I_m}{qV} + g_0(n_0 - n_{tr})n_{pm} - an_{p0}n_m - \frac{n_m}{\tau}\right)$$

for this, it is similarly expressed modulation terms as

$$\frac{dn_m}{dt} = \frac{I_m}{qV} + g(n_0)n_{pm} - g_0 n_{p0} n_m - \frac{n_m}{\tau} \tag{2-11}$$

$$\frac{dn_{pm}}{dt} = g_0 n_{p0} n_m + g(n_0)n_{pm} - \frac{n_{pm}}{\tau_p} \tag{2-12}$$

The small signal terms in frequency domain of carrier and photon are given

by

$$n_m(t) = n_m(\omega)e^{j\omega t}$$

$$n_{pm}(t) = n_{pm}(\omega)e^{j\omega t}$$

substitute into Eq. (2-11) and (2-12), the equations become

$$j\omega n_m(\omega)e^{j\omega t} = \frac{I_m(\omega)e^{j\omega t}}{qV} + g(n_0)n_{pm}(\omega)e^{j\omega t} - g_0 n_{p0} n_m(\omega)e^{j\omega t} - \frac{n_m(\omega)e^{j\omega t}}{\tau}$$

Carrier modulation term in frequency domain is simplified as

$$j\omega n_m(\omega) = \frac{I_m(\omega)}{qV} + g(n_0)n_{pm}(\omega) - g_0 n_{p0} n_m(\omega) - \frac{n_m(\omega)}{\tau}$$

$$\left(j\omega + g_0 n_{p0} + \frac{1}{\tau}\right) n_m(\omega) = \frac{I_m(\omega)}{qV} + g(n_0)n_{pm}(\omega) \tag{2-13}$$

Photon modulation term in frequency domain is simplified as

$$j\omega n_{pm}(\omega) = g_0 n_{p0} n_m(\omega) + g(n_0)n_{pm}(\omega) - \frac{n_{pm}(\omega)}{\tau_p}$$

$$\left(j\omega - g(n_0) + \frac{1}{\tau_p}\right) n_{pm}(\omega) = g_0 n_{p0} n_m(\omega) \tag{2-14}$$

Solve for $n_m(\omega)$ and $n_{pm}(\omega)$ using Eq. (2-13) and (2-14), we obtain the frequency response of two arranged equations as below

$$n_m(\omega) = \left(\frac{j\omega}{j\omega\Omega - \omega^2 - \omega_r^{\,2}}\right)\left(\frac{I_m(\omega)}{qV}\right) \tag{2-15}$$

$$n_{pm}(\omega) = \left(\frac{\tau_p \omega_r^{\,2}}{j\omega\Omega - \omega^2 - \omega_r^{\,2}}\right)\left(\frac{I_m(\omega)}{qV}\right) \tag{2-16}$$

where

$$\omega_r^2 = (2\pi \cdot f_r)^2 = \left(\frac{n_{p0}}{\tau_p}\right) g_0 \qquad \text{……Relaxation frequency} \qquad (2\text{-}17)$$

$$\Omega = \frac{1}{\tau} + n_{p0} g_0 \qquad \text{……Damping constant (decay rate)} \qquad (2\text{-}18)$$

With the Eq. (2-15) and (2-16) we observe the coupling between the small signal photon, n_{pm}, and carrier, n_m. Small signal carrier injection induces photon achieved oscillation. This phenomenon produces a natural resonance in the laser cavity which shows up the output power of the laser in response to sudden changes in the input current. The natural frequency of oscillation associated with this mutual dependence between n_m and n_{pm}. Modulation response is expanded the small signal modulation relationship to steady-state. From Eq. (2-15) and (2-16), the modulation response is denoted as

$$M(\omega) = \left|\frac{n_{pm}(\omega)}{n_{pm}(0)}\right| = \left|\frac{\dfrac{\tau_p \omega_r^2}{j\omega\Omega - \omega^2 - \omega_r^2}}{\dfrac{\tau_p \omega_r^2}{\omega_r^2}}\right| = \left|\frac{\omega_r^2}{j\omega\Omega - \omega^2 - \omega_r^2}\right| \qquad (2\text{-}19)$$

The general behavior of $M(\omega)$ is shown in Figure 2-6. Modulation bandwidth is determined as cutoff frequency, f_c, which is the position with half response written as

$$M(\omega_c) = \frac{1}{2} M(0) = \frac{1}{2} \frac{\omega_r^2}{\left[\left(\omega_c^2 - \omega_r^2\right)^2 + \omega_r^2 \Omega^2\right]} = \frac{1}{2} \qquad (2\text{-}20)$$

for $\omega_r^2 \Omega^2 << (\omega_c^2 - \omega_r^2)^2$, the cutoff frequency, ω_c, is approximated to $\sqrt{3}\,\omega_r$.

Transfer function, $H(\omega)$, is the identical term in Eq. (2-11) and (2-12)

respectively obtained with Cramer's rule. It is similar to modulation response, *M(ω)*, describing the response of the laser intensity to small variations in the drive current through the active region. That is,

$$H(f) = C\frac{f_r^{\,2}}{f_r^{\,2} - f^2 + j\frac{f}{2\pi}\gamma} \tag{2-21}$$

where f_r is the resonance frequency same as Eq. (2-17), γ is the damping rate similar to Eq. (2-18), and C is a constant. Accounting for additional extrinsic limitations due to carrier transport and parasitic elements related to the laser structure results in an extra pole in the small signal modulation transfer function

$$H(f) = C\left(\frac{f_r^{\,2}}{f_r^{\,2} - f^2 + j\frac{f}{2\pi}\gamma}\right)\cdot\left(\frac{1}{1 + j\frac{f}{f_p}}\right) \tag{2-22}$$

where f_p is the cutoff frequency of the low pass filter characterizing the extrinsic limitations. It is crucial for microwave applications that the modulation bandwidth of the VCSEL is sufficiently large so that efficient modulation is achieved as the modulation frequency.

2-3 Scattering parameters

For microwave signal measurement, direct power measurement becomes prevalent in most applications because voltage and current measurements become unrealistic. One reason for this is that voltage and current may vary with position along a lossless transmission line but power maintains a constant value. Another is in transmission line configurations where voltage and current are more difficult to define. For these reasons, at radio and microwave frequencies,

power is more easily measured than voltage or current as a fundamental quantity. Thus, the measurement of incident, reflected, and transmitted electromagnetic wave is involved as lightwave analogy, is shown in Figure 2-7. Network analyzer can accurately measure the incident, reflected, and transmitted energy that is launched onto a transmission line, reflected back to the source due to impedance mismatch, and successfully transmitted to the terminating device.

In order to satisfy an unknown two-port device, we must make measurement computed by a set of parameters, which can be used to describe the electrical behavior of our device. Scattering parameters (S-parameters) measurement is better method at high frequency. These parameters relate to familiar measurement such as gain, loss, and reflection coefficient. That is,

$$\begin{bmatrix} b_1 \\ b_2 \end{bmatrix} = \begin{bmatrix} S_{11} & S_{12} \\ S_{21} & S_{22} \end{bmatrix} \cdot \begin{bmatrix} a_1 \\ a_2 \end{bmatrix} \tag{2-23}$$

Where a_1 and a_2 are incident signal, b_1 and b_2 are signal received of each ports, and S-parameters are determined by measuring the magnitude and phase of incident, reflected, and transmitted signals. A simple two-port network is illustrated as Figure 2-8.

2-4 Summary

High-speed characteristics of VCSEL can be resolved by injection and light output power of small signal modulation. Modulation response is a concept as gain which can be measured as parameter S_{21}. Parameter S_{11} is equivalent to the input complex reflection coefficient or impedance of the device. S_{21} and S_{11} are useful to analyze effect of high-speed characteristics upon process structures, and benefit to establish an equivalent circuit as VCSEL for impedance matching work. In Chapter 4, we will present the measurement result and circuit modeling in detail.

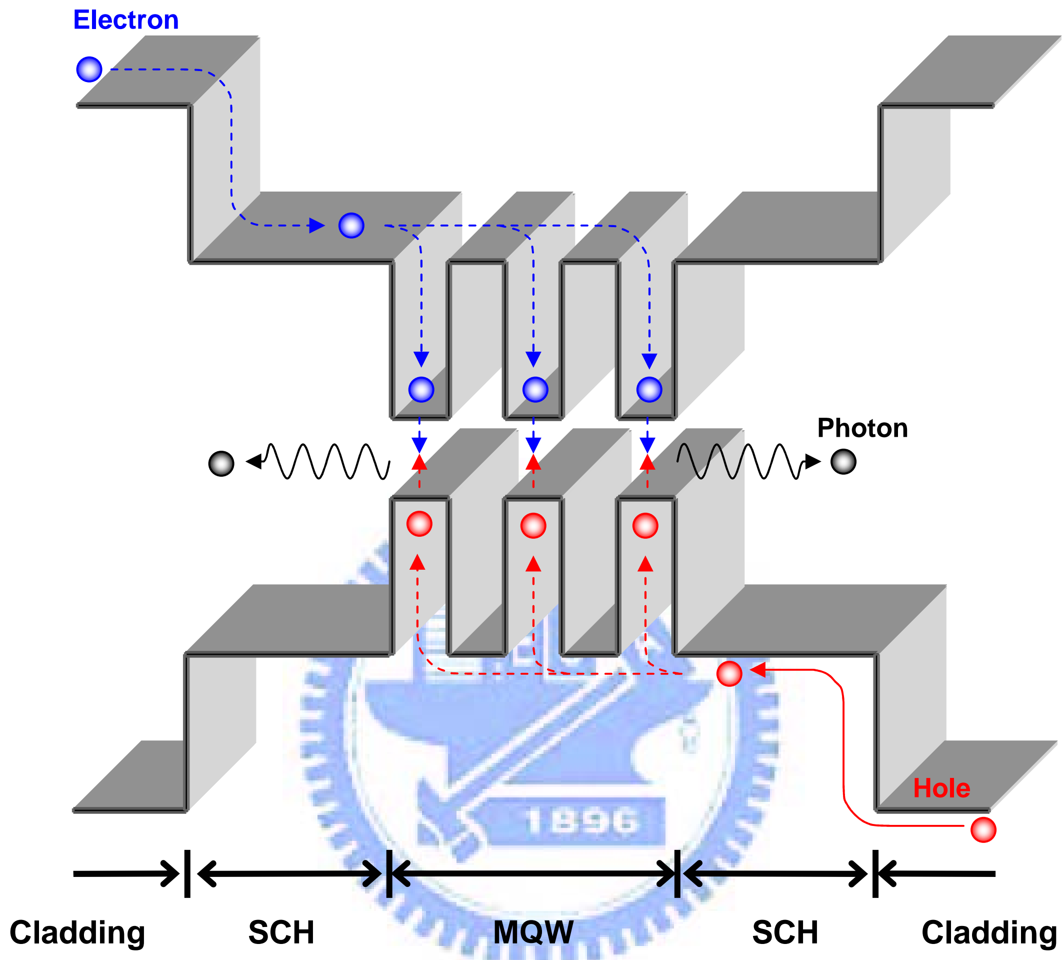

Figure 2-1 Band diagram of active region of VCSEL

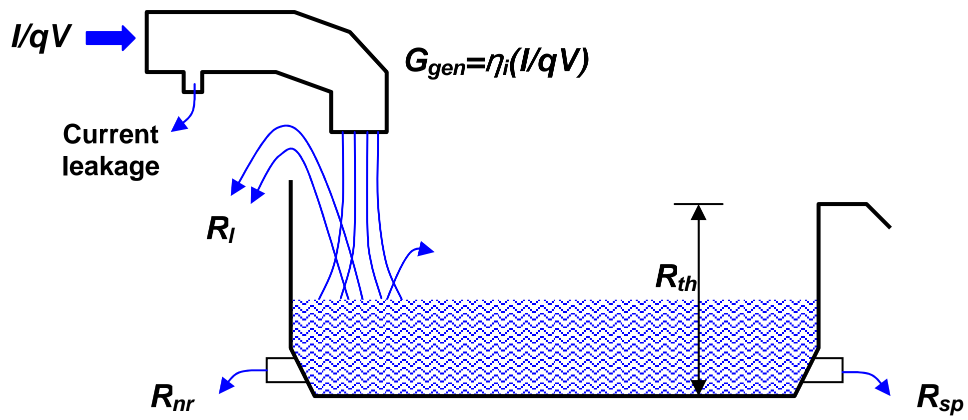

(a)

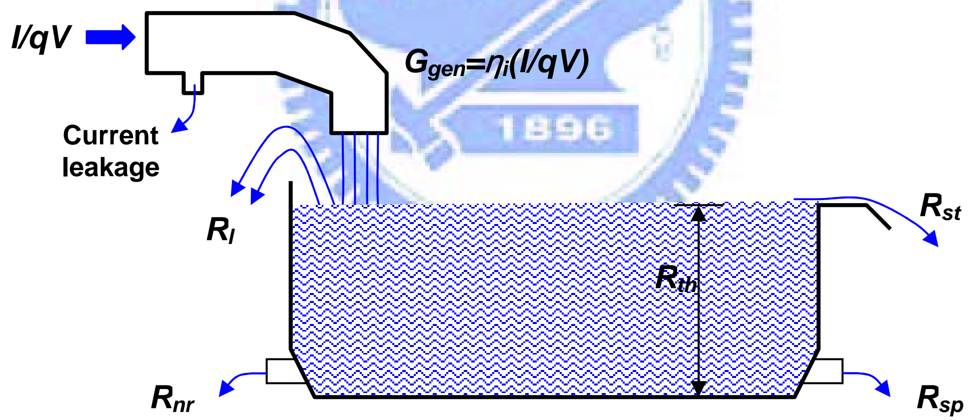

(b)

Figure 2-2 Reservoir analogy (a) under threshold (b) above threshold

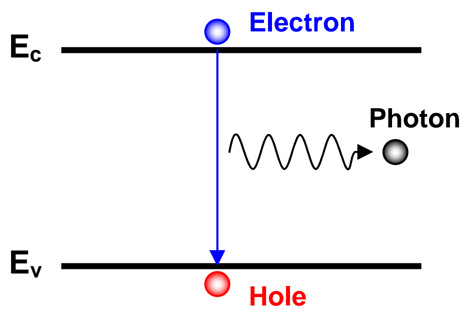

(a) Spontaneous emission

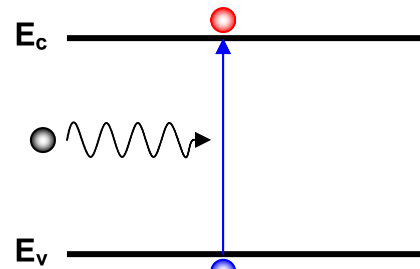

(b) Stimulated generation (absorption)

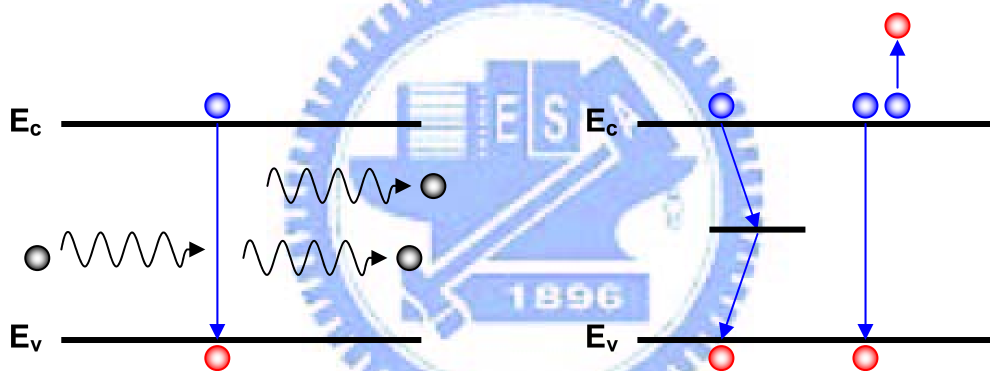

(c) Stimulated recombination (emission)

(d) Nonradiative recombination

Figure 2-3 Basic electronic recombination/generation mechanism

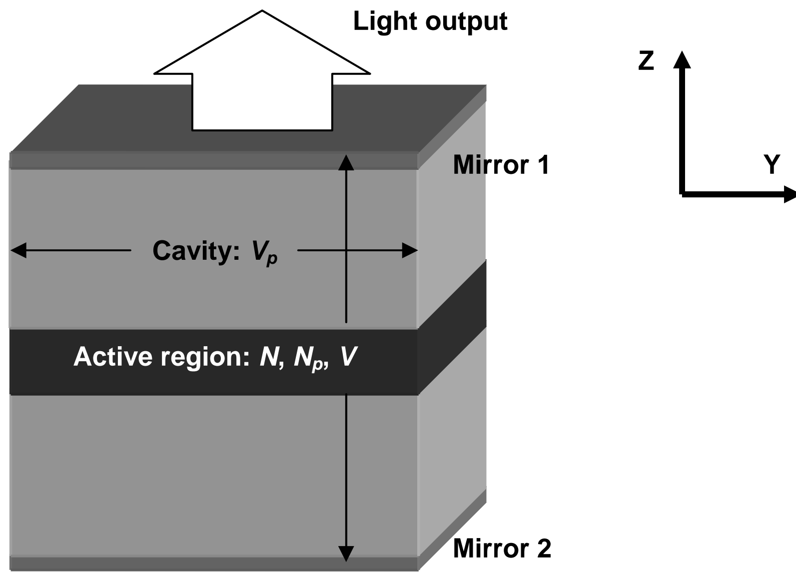

Figure 2-4 Schematic of VCSEL illustrating active region and cavity volumes

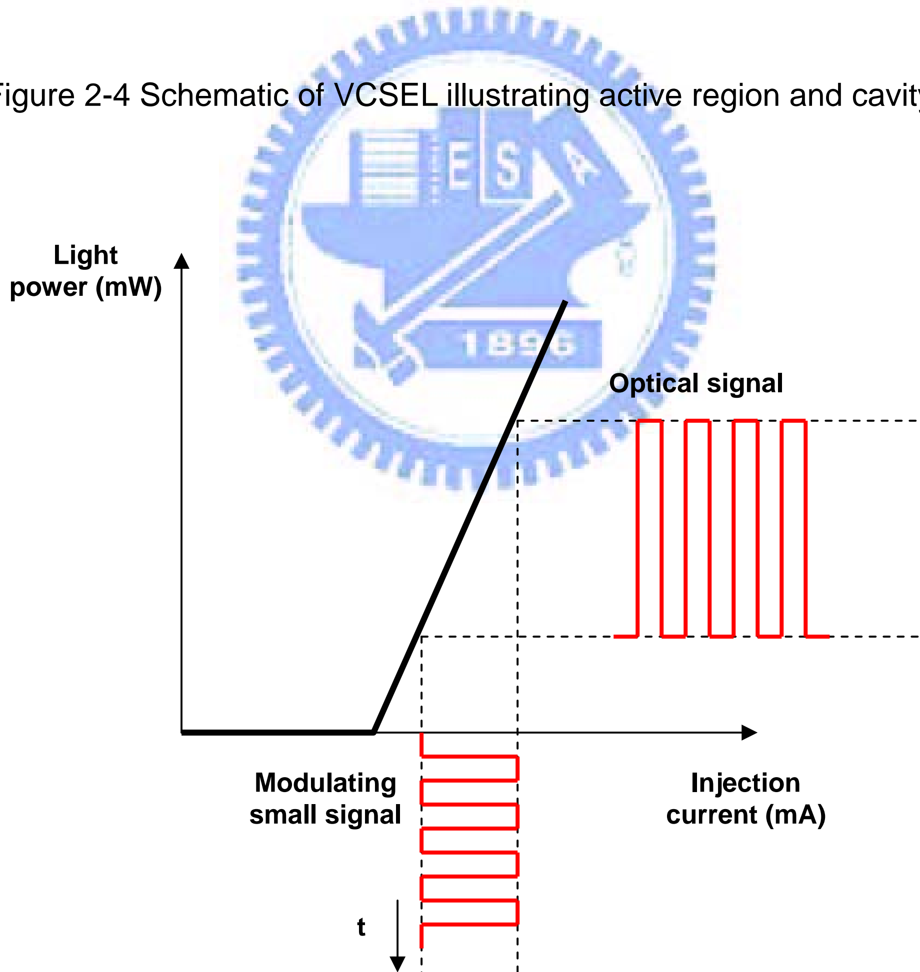

Figure 2-5 Conversion from electrical small signal train into optical signal

1896

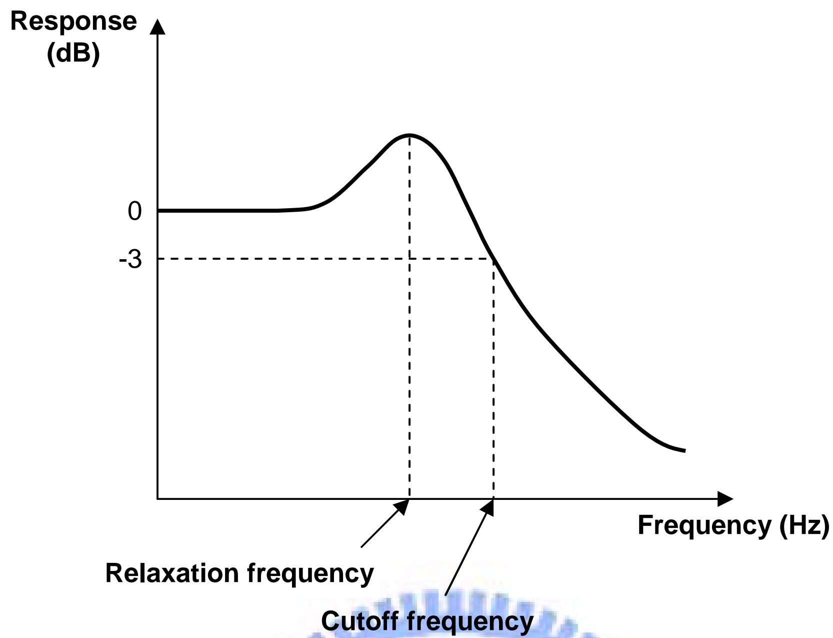

Figure 2-6 Small signal modulation response of a VCSEL

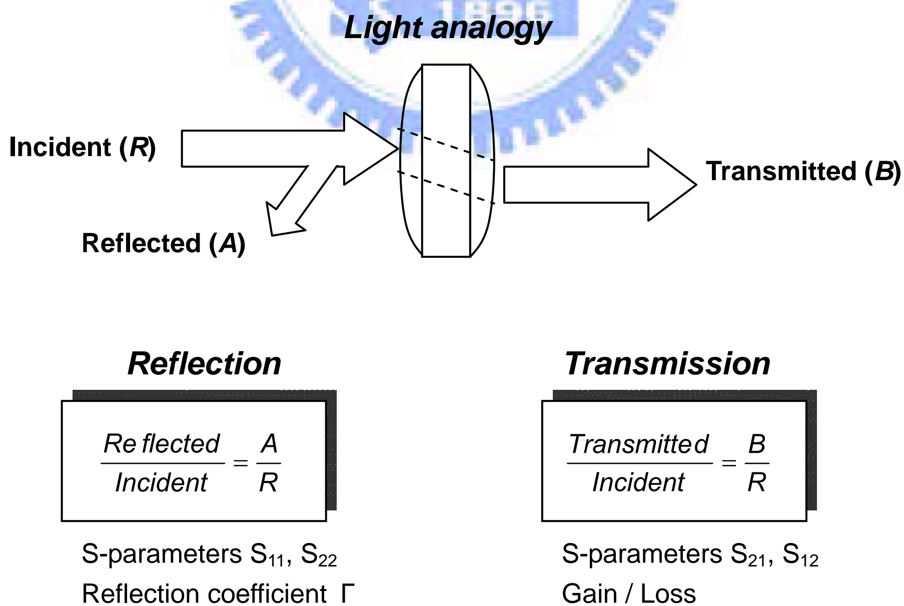

Reflection	*Transmission*
$\frac{Reflected}{Incident} = \frac{A}{R}$	$\frac{Transmitted}{Incident} = \frac{B}{R}$
S-parameters S_{11}, S_{22}	S-parameters S_{21}, S_{12}
Reflection coefficient Γ	Gain / Loss

Figure 2-7 Common terms for high-frequency device characterization

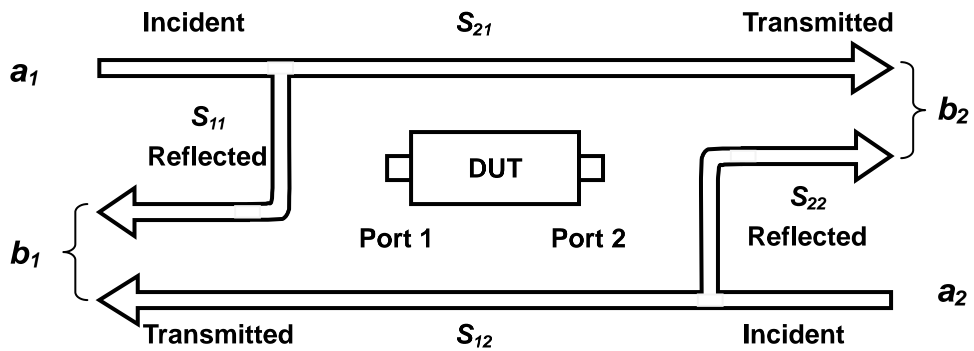

Forward

$$S_{11} = \frac{Reflected}{Incident} = \frac{b_1}{a_1}\bigg|_{a_2=0}$$

$$S_{21} = \frac{Transmitted}{Incident} = \frac{b_2}{a_1}\bigg|_{a_2=0}$$

Reverse

$$S_{22} = \frac{Reflected}{Incident} = \frac{b_2}{a_2}\bigg|_{a_1=0}$$

$$S_{12} = \frac{Transmitted}{Incident} = \frac{b_1}{a_2}\bigg|_{a_1=0}$$

Figure 2-8 A simple two-port network is defined as S-parameters

Chapter 3

VCSEL design and measurement setup

In this chapter, we presented the fabrication method of VCSEL, instrument setup for electrical and optical characteristics measurement. The fabrication techniques for VCSEL such as air-post, regrowth, proton-implantation and selective oxidation had been employed to define the current path, gain region, carrier and the optical confinement. With in these techniques, the VCSEL fabricated by proton-implantation and selective oxidation had some superior properties such as simple and stable process. The design principles of VCSEL wafer structure were based on the method described as follow section. Finally, probe station system, spectrum measurement system and the establishments of RF measurement system were described as follows.

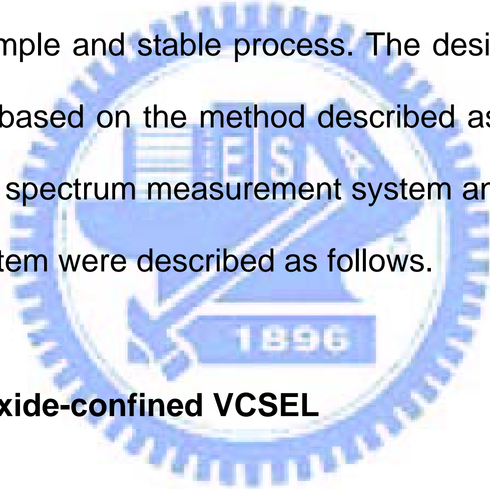

3-1 Fabrication of oxide-confined VCSEL

A vertical cavity surface emitting laser consisted of multi-quantum-well sandwiched between two highly reflective distributed Bragg reflectors (DBRs). The 850nm GaAs / AlGaAs VCSEL devices studied here were grown by MOCVD on the Si-doped GaAs substrate. The bottom DBR had 32 pairs of alternating $Al_{0.15}Ga_{0.85}As$ / $Al_{0.9}Ga_{0.1}As$ pairs with quarter-wavelength-thick layer. The active region was consisted of three GaAs / AlGaAs quantum wells and cladding layer. The top DBR had 22 pairs of alternating $Al_{0.15}Ga_{0.85}As$ / $Al_{0.9}Ga_{0.1}As$ layer. A high Al-content selective oxidation layer, $Al_{0.98}Ga_{0.02}As$, was inserted just three layers above the active region. The VCSEL structure was

trenched a ring of mesa, indicated in Figure 3-1, in order to execute oxidation process, which still improved current spreading effect. A bridge connected with contact ring and bond pad for current injection. Mesa structure benefited reducing current path and inducing optical confinement. Passivation layer coating, used of SiNx, formed an isolation layer reducing leakage current below metal contact. The detailed process of oxide-confined VCSEL was desired as Figure 3-2.

The scheme of oxidation process system was drawn in Figure 3-3. The VCSEL was placed into center of furnace and purge by N2. The furnace annealed approach 420°C then imported the invariable flow-rate of steam into furnace for fixed time. Oxidation time was crucial for the process for forming different oxide apertures. The oxide-extent was almost linear relative to oxidation time, shown in Figure 3-4. Here we processed different mesa structure to fabricate designed oxide aperture by fixed oxidation time. By the method, we could fabricate series oxide aperture VCSEL stably, as 6, 7 and 8 μm. Photograph of oxide VCSELs were taken by CCD as Figure 3-5.

3-2 Fabrication of oxide-implant VCSEL

The process was similar to oxide-confined VCSEL. The process of proton-implantation, indicated in Figure 3-6, was done at energy of 300-420 KeV with dosage of 10^{15} cm^{-2} behind coating p-metal. Different bombarding energy was purposed to create partial rectangular isolating region under the P-metal. Simulation result with Trim software was shown in Figure 3-7. The implantation window is designed away from oxide aperture to avoid triggering the reliability

issue. A series VCSELs with different oxide aperture size were fabricated in the same implant process condition and their static and dynamic characteristics in were presented in chapter 4.

3-3 Probe station and spectrum measurement system

Probe station system was essential instrument for basic characteristics measurement such as I-L (current versus light output), I-V (current versus voltage). Scheme of probe station system, illustrated in Figure 3-8, contained probe station, current source, and power-meter module. Keithley 238 as current source supplies continuous current for diode laser and receives relative voltage synchronously. Laser output power is measured by Newport power-meter module (model 1835C). With these data, we could plot the trend of L-I-V associated with computer. For accuracy power measurement, an integration sphere was used to pick up whole light output from VCSEL.

For basic measurement, VCSEL device was placed on platform of probe station and injected bias current with microprobe. We could observe threshold condition, slope efficiency, turn-on voltage and differential resistance as L-I-V information by sweeping bias current injection. Distribution of transverse mode power is metered as near-field pattern. Near-field pattern (NFP) is still obtained by specific CCD and traces out results with computer. Beam-view analyzer is useful software we used in taking NFP. We could obtain NFP image under threshold, as spontaneous emission, to define oxide aperture size.

Emission spectrum was measured by Advantec optical spectrum analyzer

(OSA). We served a multi-mode fiber bundle on probe close to emission aperture in focus for taking spectra. OSA had small spectrum resolution as 0.1nm for accurately measuring VCSEL lasing spectrum. Scheme of spectrum measurement system was combined with probe station as Figure 3-8.

3-5 Microwave test system

Whole microwave test system mainly contained network analyzer, optical platform and microwave probe, illustrated with Figure 3-9. Agilent 8720ES network analyzer was a crucial instrument of this microwave measurement. Transmitter of network analyzer produced -10dBm RF signal. Laser diode drivers (Newport, model 525) provided direct current signal to set the laser above the threshold. Bias-Tee combined AC and DC signal transmission through the same coaxial cable. The mixed signal was through the coplanar microwave probe injecting into VCSEL, which was bonded on sub-mount substrate as Figure 3-10. Coplanar microwave probe had 700μm pitch (ground (G) to signal (S) tip spacing) and suitable frequency range was up to 40 GHz. Signal probe was higher than ground tips. Fine probing was observed by signal probe skating on contact substrate.. Illustration of microwave probe holder in whole was shown in Figure 3-11.

Optical platform contained microscope, beam splitter, objective and fiber coupler etc.. We used a long work distance objective (20X, Mitutoyo), fixed in a triple-divide translation stage, to pick up the laser output from VCSEL. Light was separated by beam splitter and received by CCD and another 10X objective (Olympus). One of splitting light was received by a simplified microscope, which

was constructed by beam splitter and CCD to make probing easily. Another light path trough 10X objective coupling into multimode fiber by five-axis fiber aligner (Newport).

The collected light was transmitted into 12 GHz photodetector (Model 1580, NewFocus) and was conversed into electrical signal and fed to network analyzer. Comparing two channels microwave signal by network analyzer, information of transmission and reflection characteristics could be expressed as vector (magnitude and phase), scalar (magnitude only), or phase-only quantities, that was, S-parameter. The theorem of S-parameter was briefly reviewed in chapter 2.

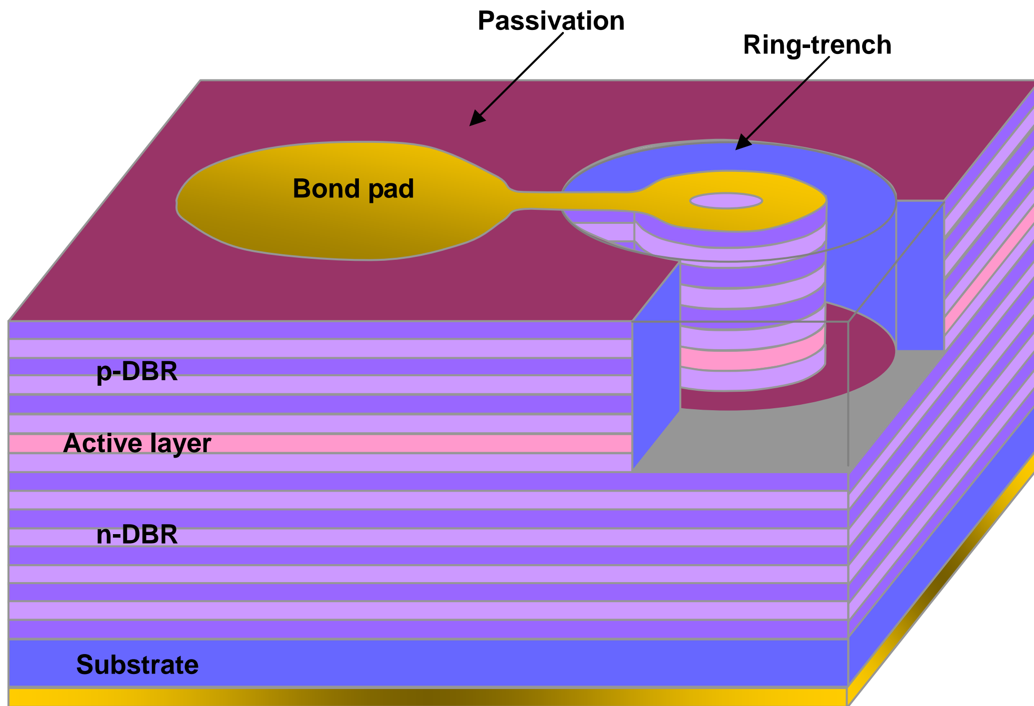

Figure 3-1 Cross section structure of ring-trenched VCSEL structure

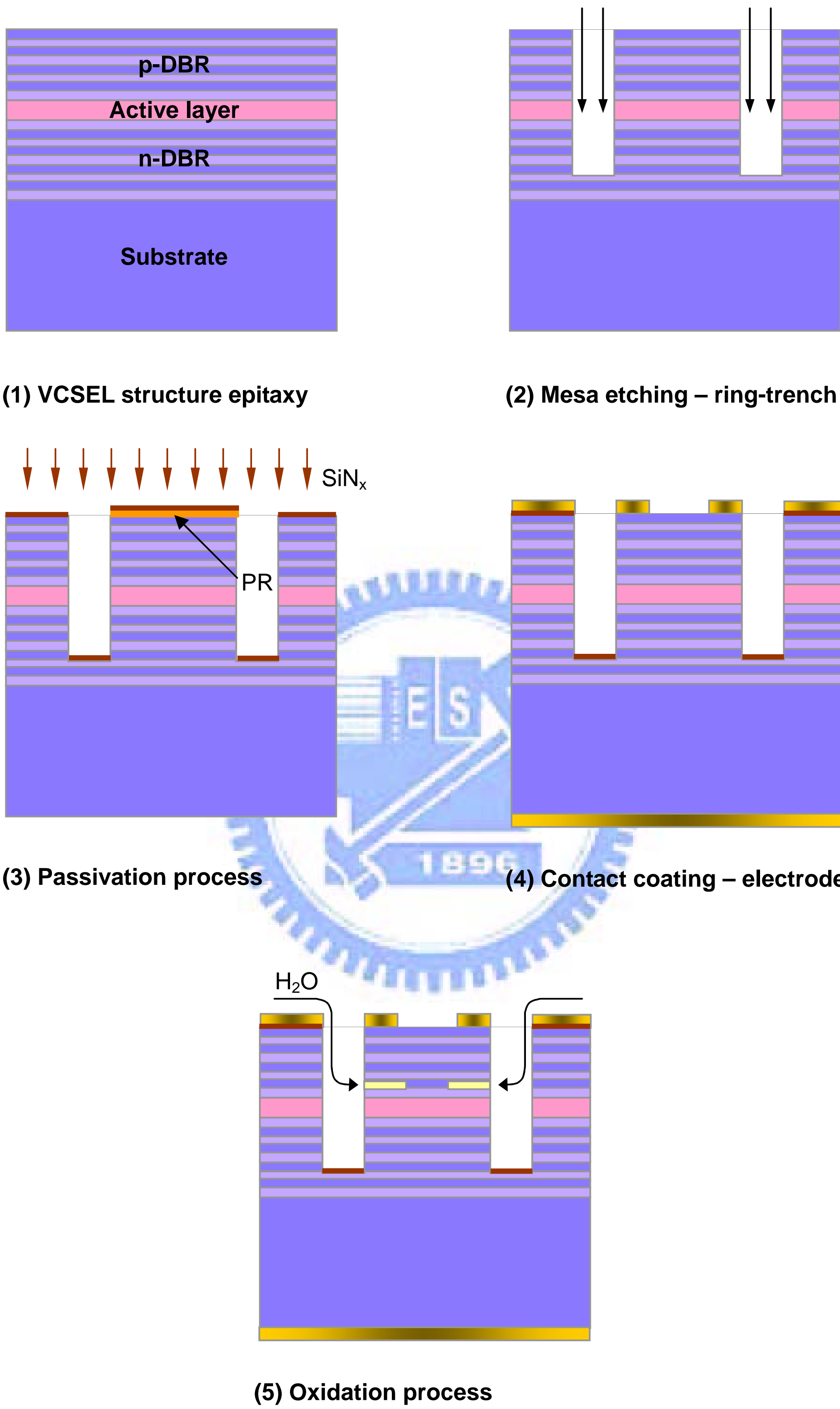

Figure 3-2 Steps of oxide-confined VCSEL process

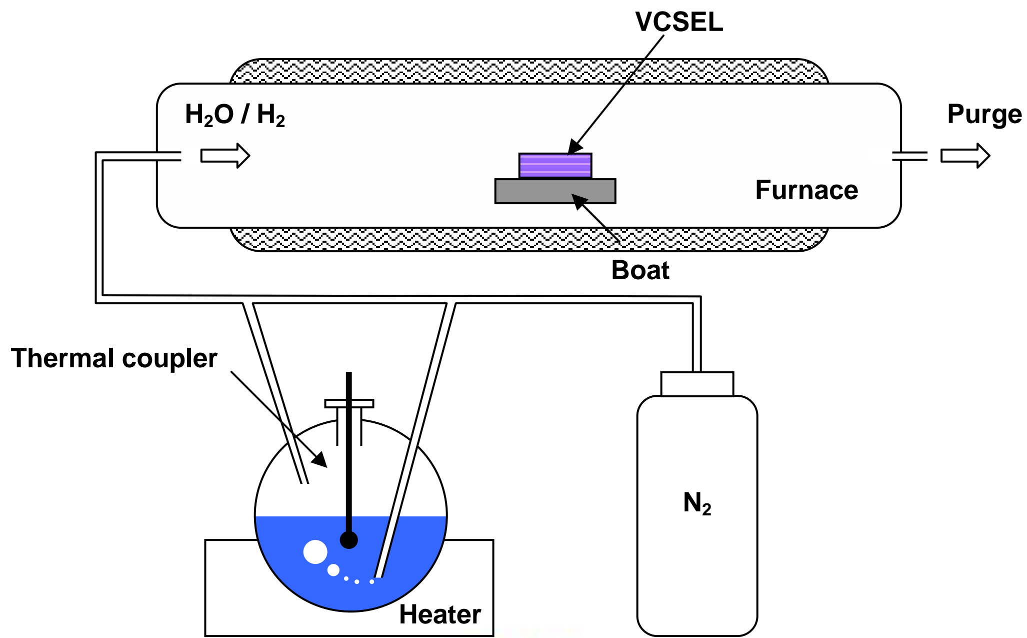

Figure 3-3 Illustration of oxidation process system setup

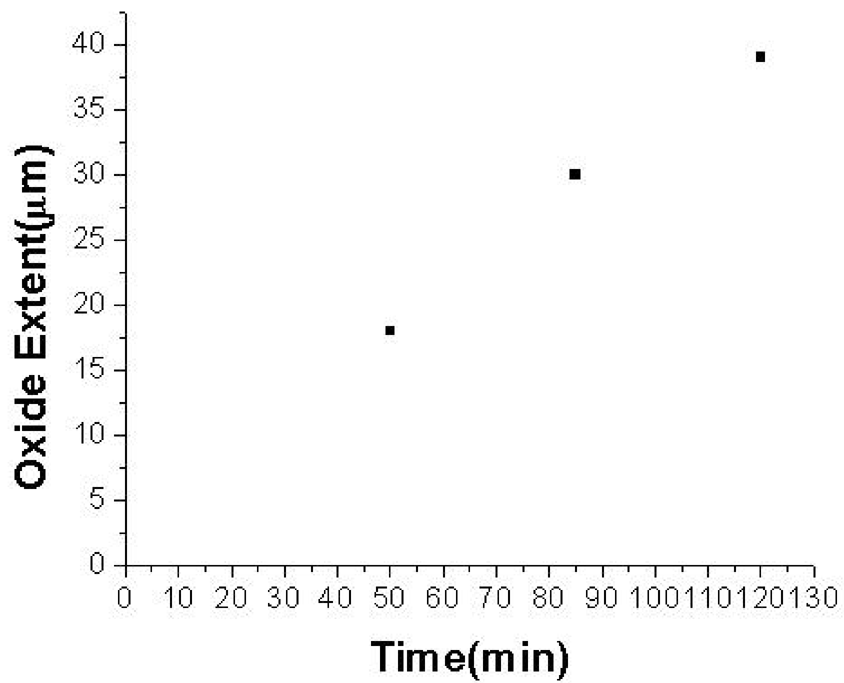

Figure 3-4 Oxidation rate of 98% Al-content layer

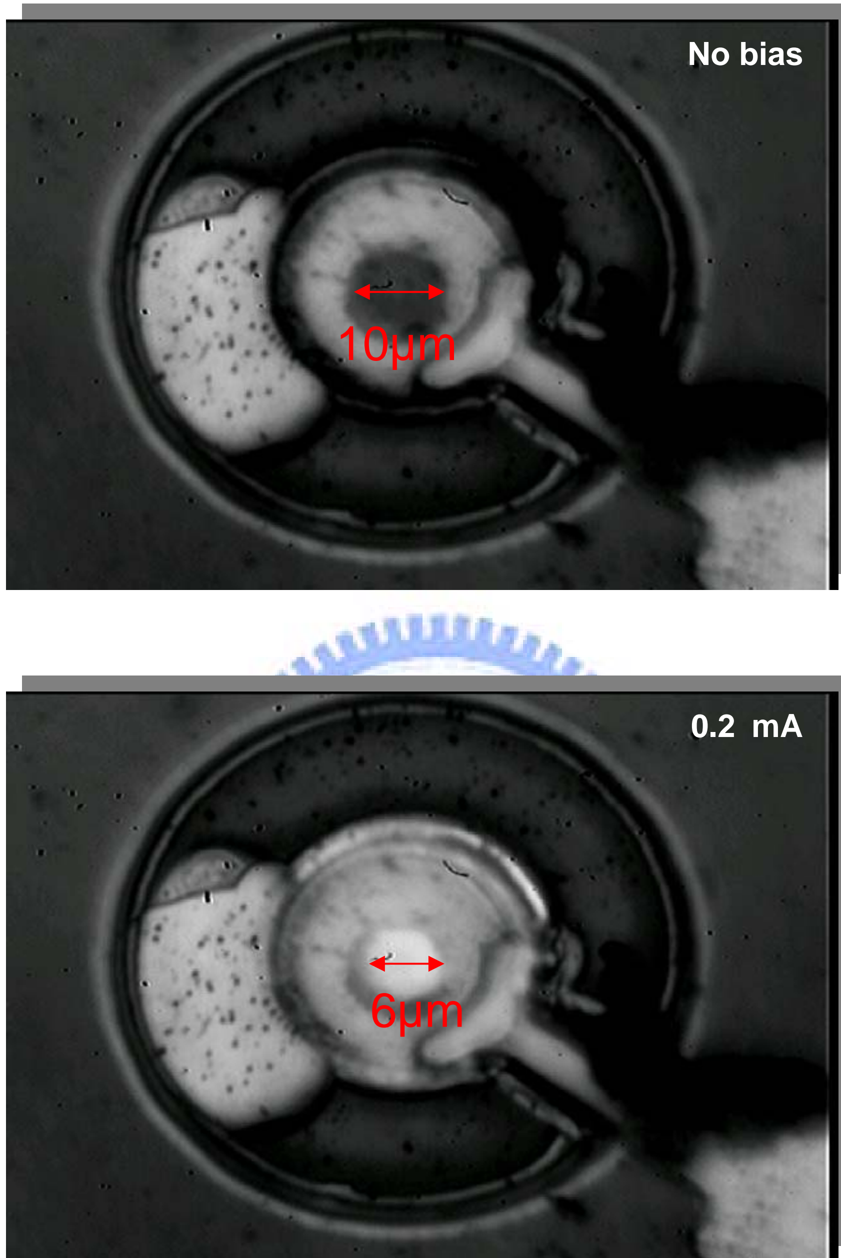

Figure 3-5 OM-image of VCSEL with 6μm oxide-aperture

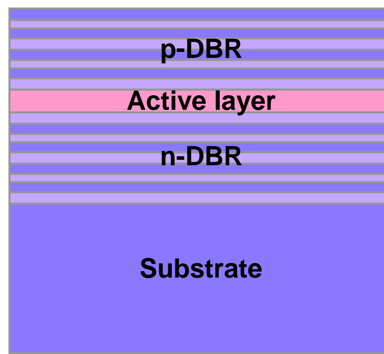

(1) VCSEL structure epitaxy

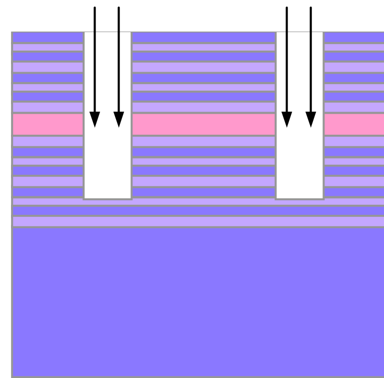

(2) Mesa etching – ring-trench

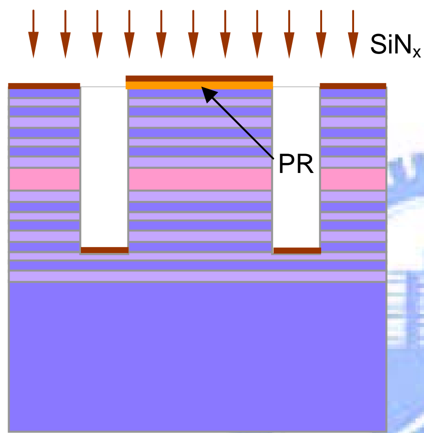

(3) Passivation process

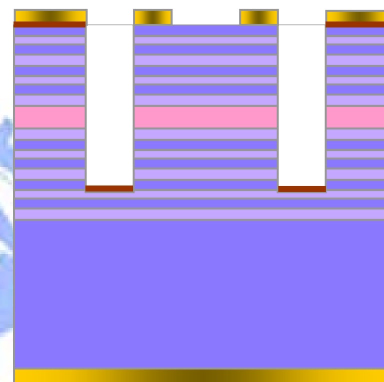

(4) Contact coating – electrode

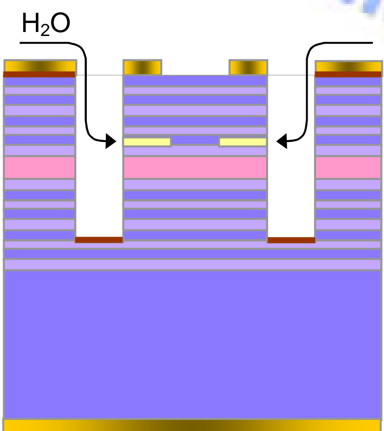

(5) Oxidation process

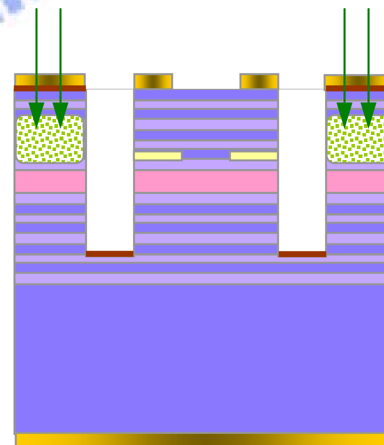

(6) Proton bombing

Figure 3-6 Steps of oxide-implant VCSEL process

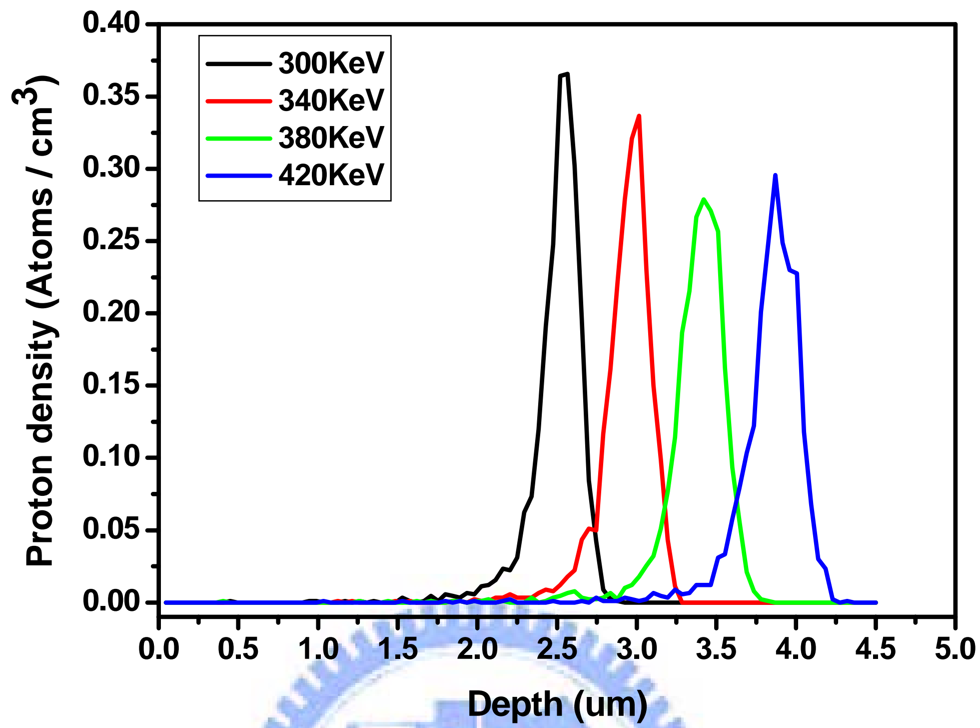

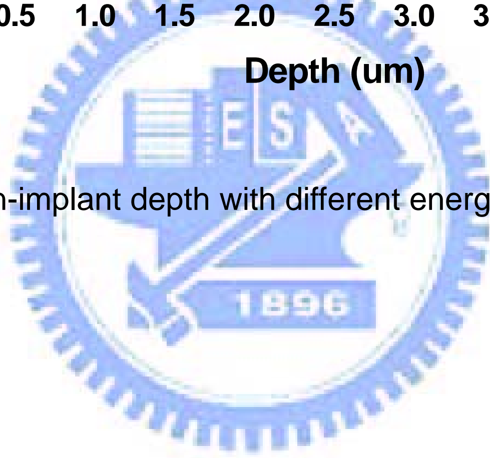

Figure 3-7 Proton-implant depth with different energy simulating by Trim

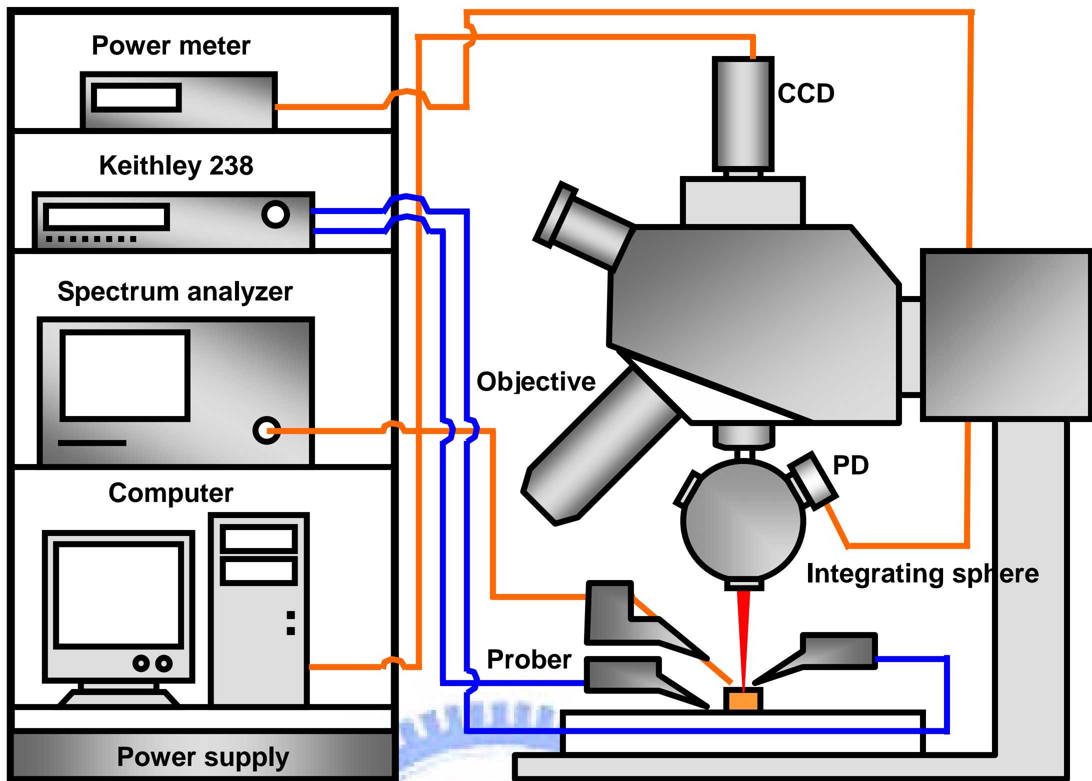

Figure 3-8 Probe station measurement instrument setup

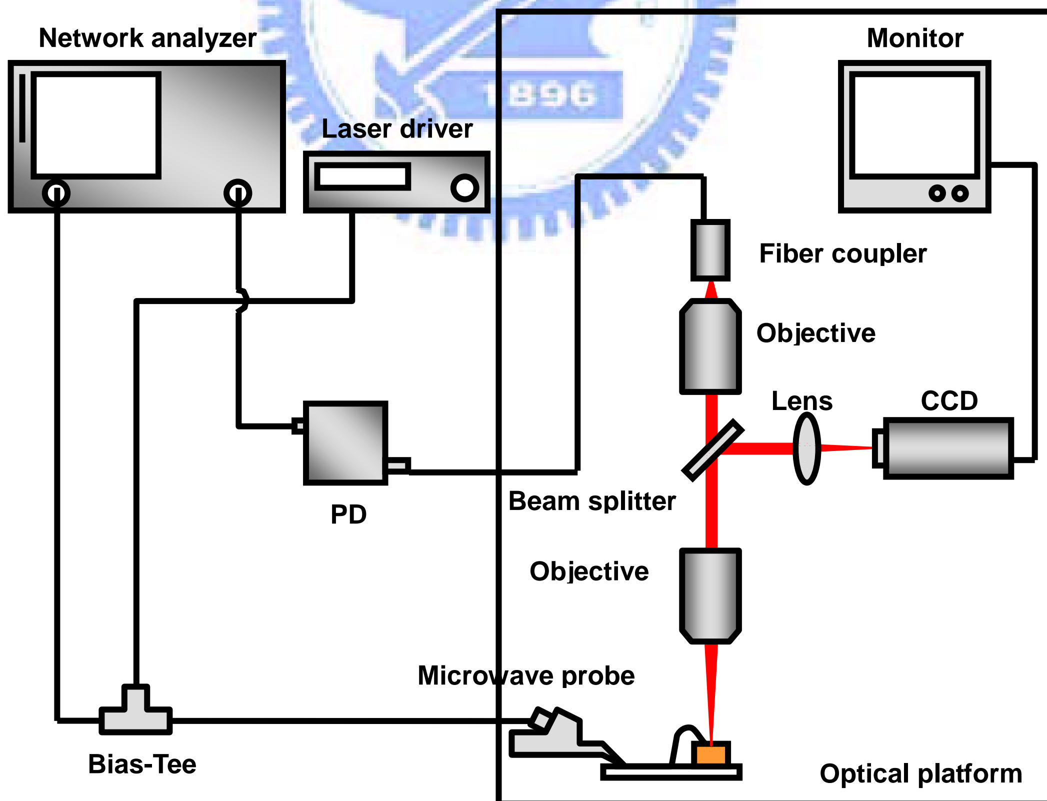

Figure 3-9 Microwave test system set-up

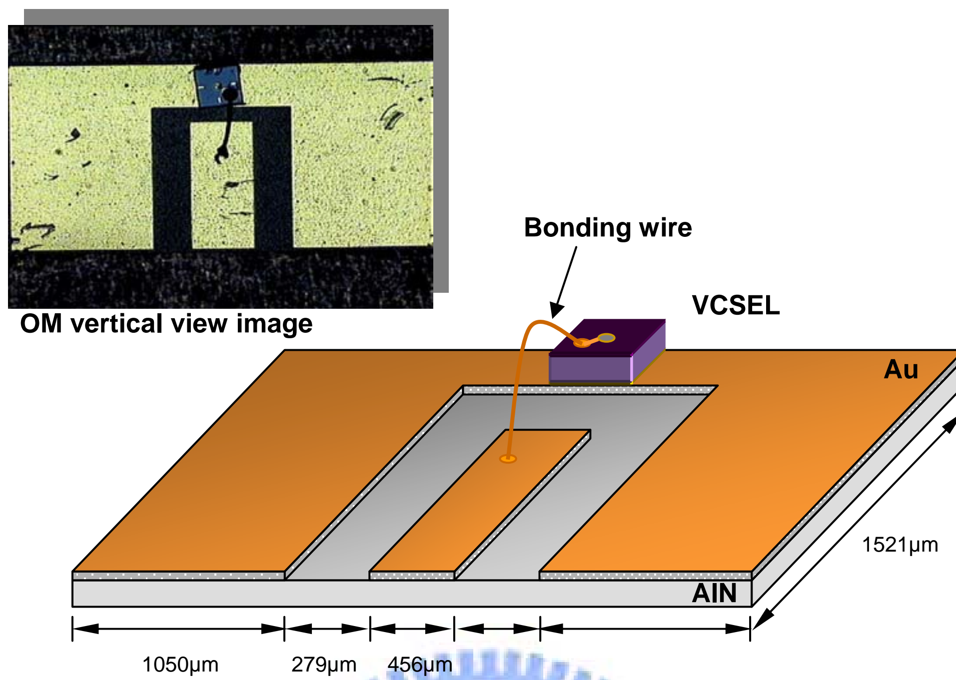

Figure 3-10 Sub-mount substrate design

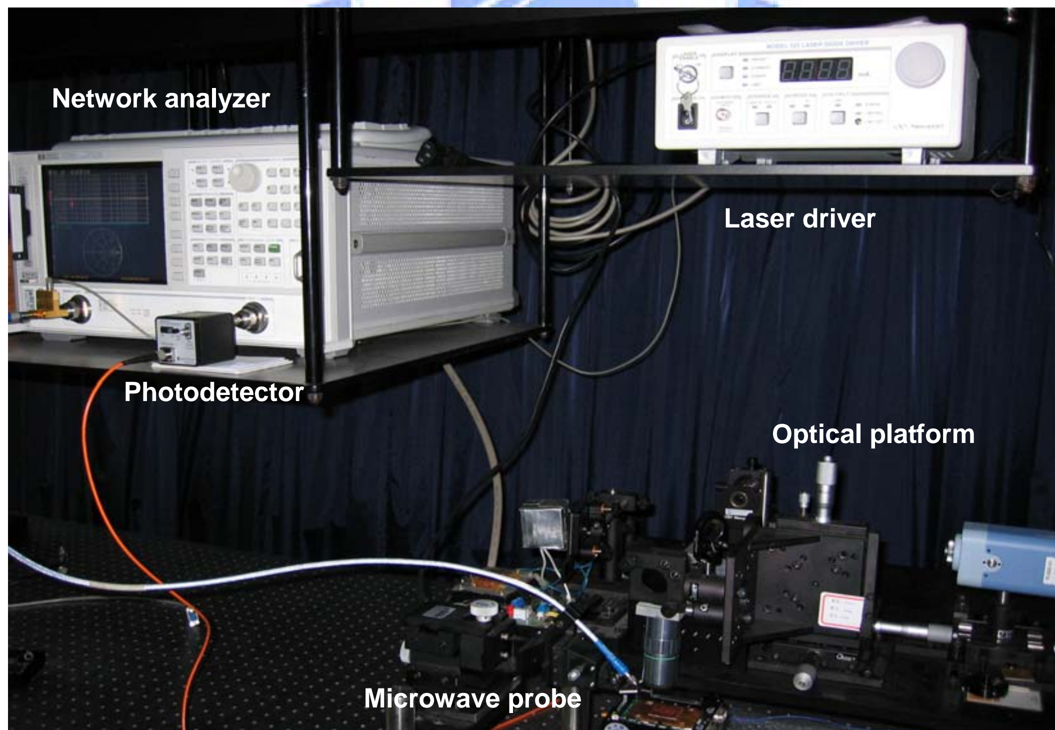

Figure 3-11 Illustration of microwave test system

Chapter 4

Measurement and modeling analysis

Oxidation process was regular process for VCSEL fabrication. Most high speed VCSEL was also made by the same method [7-8]. But only oxide-confined structure could be not enough to make device approaching high speed [9]. Parasitic capacitance was crucial parameter for speed limitation. That was, the region between bonding pad and oxide-layer formed considerable capacitance. There were many efforts to reduce the capacitance reported based on reduction of pad area [10], mesa implantation [11], and BCB process [12-13]. Mesa implantation was commercial semiconductor process that fabrication was easier than BCB process. For this, we chose oxide-only and oxide-implant VCSELs to compare with their high speed characteristics in first section. In second section, we compared with different oxide aperture size VCSELs. Oxide aperture diameter resolved transverses mode which affected modulation speed. We still found out if NFP and spectrum width was concerned with modulation limitation. Static and high speed characteristics of these VCSELs were still investigated. Equivalent circuit modeling was investigated in section 4-3. With VCSEL modeling, the equivalent components were extracted and observe the modulation limitation caused by structure.

4-1 Comparison oxide-confined and oxide-implant VCSELs

Oxide-confined VCSEL and oxide-implant VCSEL had same process structure, shown in Figure 4-1. Process structure was described in Chapter 3. Both VCSEL had the same oxide aperture as 8 μm and mesa as 22 μm. Oxide-implant VCSEL had an isolation region as implant region was kept away from mesa to prevent damage from destroying the active region and hence voided triggering reliability issues.

The static characteristics of both VCSEL were shown in Figure 4-2. Threshold current of oxide-only and oxide-implant VCSEL was 1.4 and 2.3 mA respectively. It meant that implant process provided additional current confinement made oxide-implant VCSEL having lower threshold current. Series resistance of both was similar as 91 and 108 Ohm. Slope efficiency, defined as conversion from injection current to output power, was 0.484 and 0.337 W/A. Power conversion efficiency, indicated in Figure 4-2, appeared that oxide-implant VCSEL had higher light output up to 18%. That was, VCSEL maintained less power dissipation avoided parasitic heating which affected output power.

The measured modulation response curves for oxide-only and oxide-implant VCSELs were shown in Figure 4-3(a) and 4-3(b), respectively. The maximum modulation bandwidth of both VCSEL was 2.3 and 8.6 GHz. The roll-off as the lower frequency part of modulation response curve of oxide-only VCSEL was serious caused by parasitic effect. The resonance frequency increased with the bias current as expected. The plots in Figure 4-4 shown that,

for both different process VCSEL, proportional value of resonance frequency versus $(I-I_{th})^{1/2}$ as D-factor was 2.75 and 2.49 GHz/mA$^{1/2}$. Modulation current efficiency factor (MCEF), indicated in Figure 4-4, appeared modulation bandwidth as function of $(I-I_{th})^{1/2}$. Oxide-implant VCSEL had 3.06 GHz/mA$^{1/2}$; furthermore, bandwidth of oxide-only VCSEL was limited by parasitic effect for high current injection. Compared with both modulation responses, of oxide-only VCSEL with large capacitance, which introduced by the thin oxide layer, resulted in parasitic effect. On the other hand, the additional implantation in oxide-implant VCSEL reduced the capacitance of device without increasing the resistance much.

For commercial high speed performance testing, oxide and oxide-Implant VCSEL were measured as eye diagram shown in Figure 4-5. Eye diagram of oxide-only VCSEL shown that jitter was about 30 ps and fall-time tail touched 10Gbps mask. That was, oxide-only VCSEL could not apply to 10Gbps communication. Oxide-implant VCSEL had small jitter below 20 ps. It still had rise-time/fall-time were 44 and 54 ps respectively. For that, oxide-implant VCSEL passed 10Gbps clarified.

4-2 Comparison oxide-implant VCSELs in different oxide aperture sizes

There were three oxide aperture sizes VCSEL investigated as their high speed performance. Oxide aperture was fabricated as 6, 7, and 8 μm. The static characteristics of these VCSEL were shown in Figure 4-6. Threshold current were 0.8, 0.8, and 1.4 mA respectively. Series resistance of VCSEL was 91, 149, and 174 Ohm. It demonstrated that small device had large resistance than large

oxide aperture ones. Slope efficiency was 0.347, 0.387, and 0.484 W/A.

Small signal modulation response of different oxide aperture size of VCSEL was shown in Figure 4-7 as 6, 7, and 8 μm respectively. At lower frequency range, modulation bandwidth of small oxide aperture VCSEL was roll-off and large aperture VCSEL was flat. The difference was attributed to the additional parasitic effect. In Figure 4-8, D-factor of three VCSEL was 2.75, 4.89, and 5.14 GHz/mA$^{1/2}$. Modulation current efficiency factor (MCEF), indicated in Figure 4-8, was 3.06, 5.54, and 5.97 GHz/mA$^{1/2}$ respectively. We observed that small oxide aperture VCSEL had better D-factor but worst MCEF at high current injection. The limitation of modulation response was possible induced by parasitic effect and heating. For the three oxide aperture size VCSEL, we could find out the optimum oxide aperture size was 7μm for high speed operation.

4-3 Equivalent circuit design and modeling

We established an equivalent circuit, depended on VCSEL structure, for investigate limitation caused by parasitic effect. The opposite equivalent circuit components were defined as Figure 4-9. Oxide-only and oxide-implant VCSEL were compared their VCSEL structure using Agilent ADS software to simulating and obtained results as S-parameter, introduced in Chapter 2.

The simulated and measured data showed better fitting as Figure 4-10. The equivalent circuit components could be extracted with reflection coefficient measured by network analyzer. Reflection coefficient, S_{11}, was also determined impedance of circuit. Extraction components value was listed as Table 4-1 and

4-2 for oxide-only and oxide-implant VCSEL respectively. For this, we found that parasitic capacitance was effectively reduced due to implantation from 2 pF down to 0.36 pF, shown in Figure 4-10, but hindered current flow and increased parasitic resistance simultaneously. Even though, the trade-off had to be mode to minimize the RC product affected modulation bandwidth. For this, oxide-implant had better modulation bandwidth than oxide-only VCSEL was demonstrated.

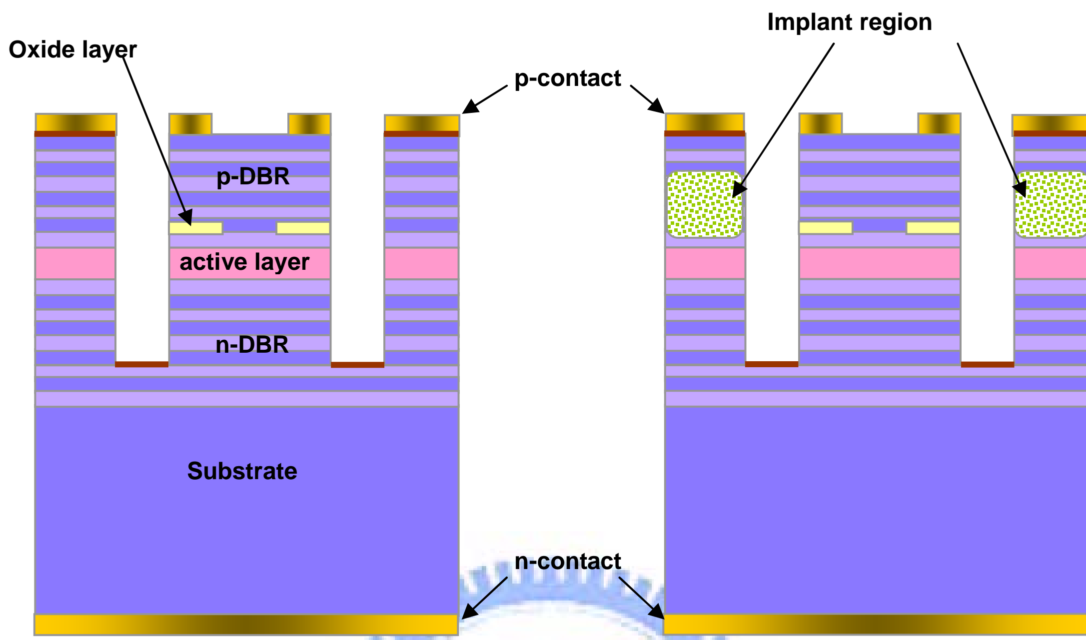

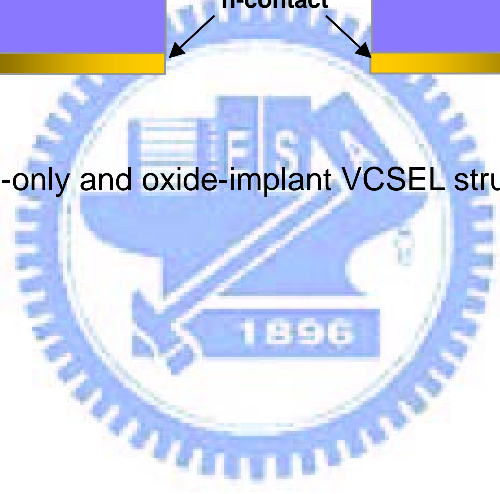

Figure 4-1 Oxide-only and oxide-implant VCSEL structure

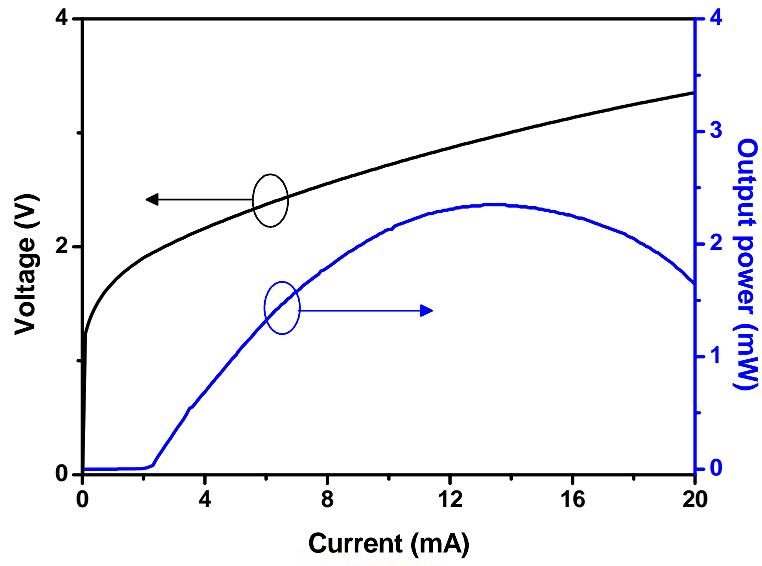

(a) Oxide-only VCSEL

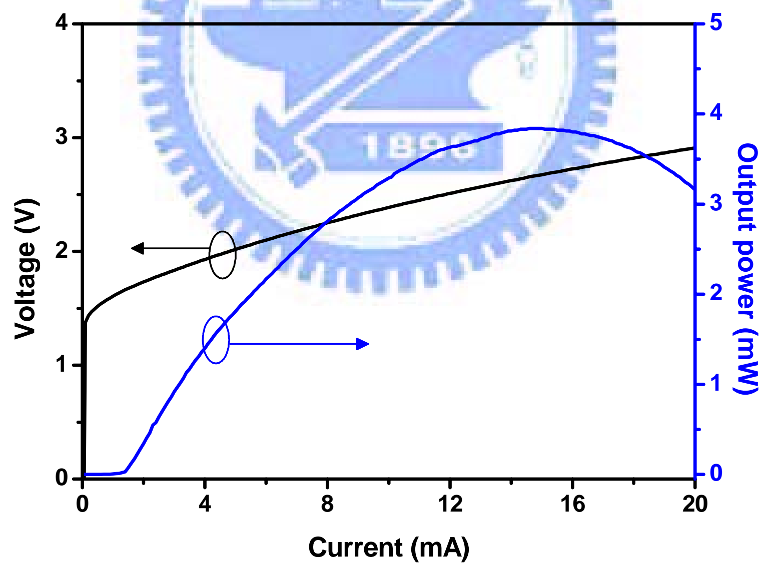

(b) Oxide-implant VCSEL

Figure 4-2 Typical LIV curve for oxide-only and oxide-implant VCSELs

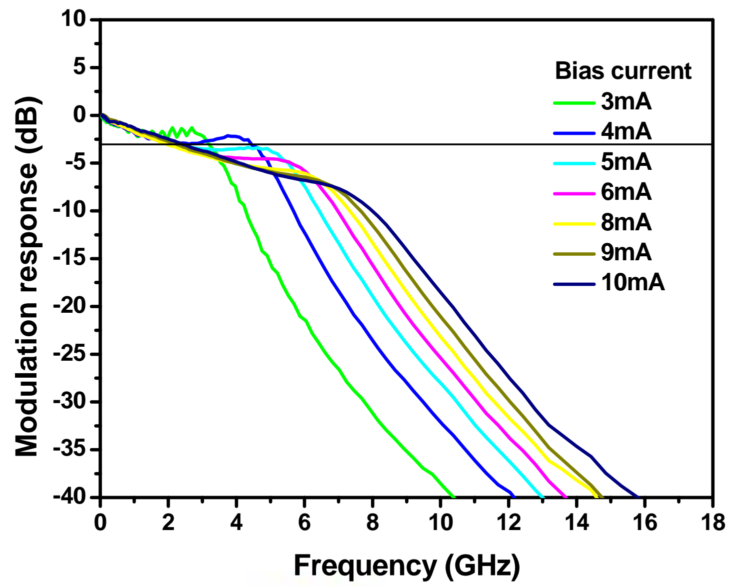

(a) Oxide-only VCSEL

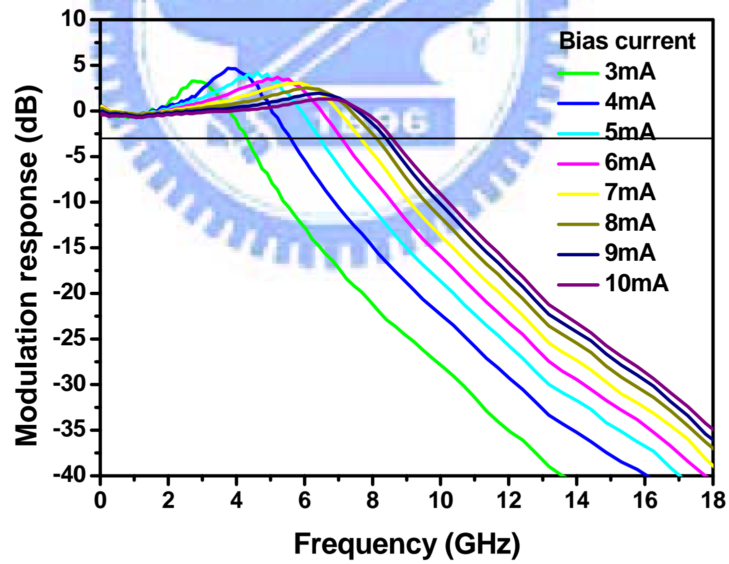

(b) Oxide-implant VCSEL

Figure 4-3 Modulation responses for both oxide-only and oxide-implant VCSELs

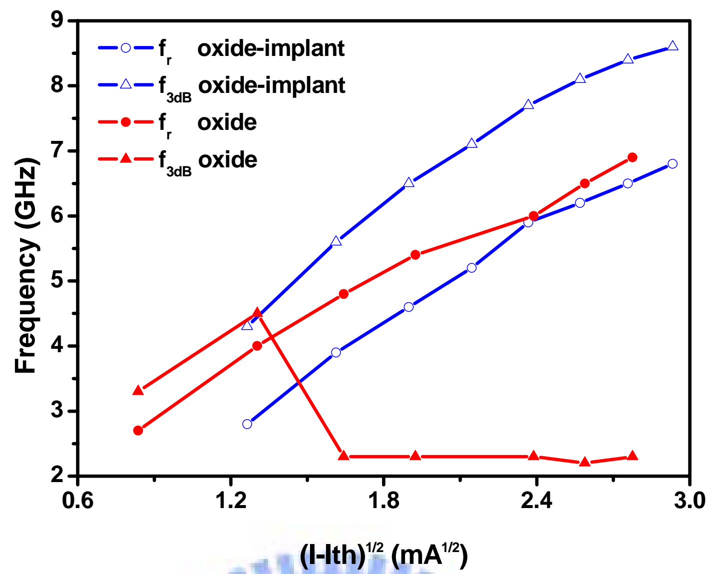

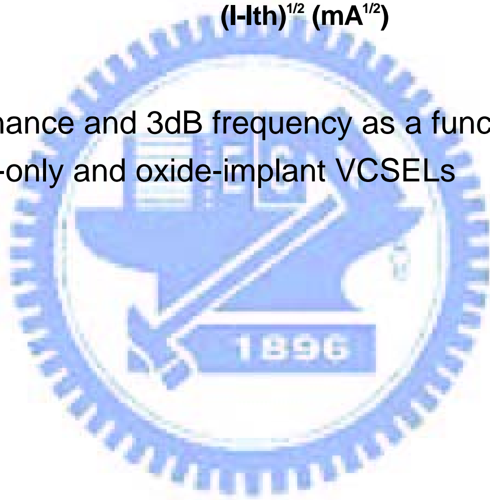

Figure 4-4 Resonance and 3dB frequency as a function of $(I\text{-}I_{th})^{1/2}$ for oxide-only and oxide-implant VCSELs

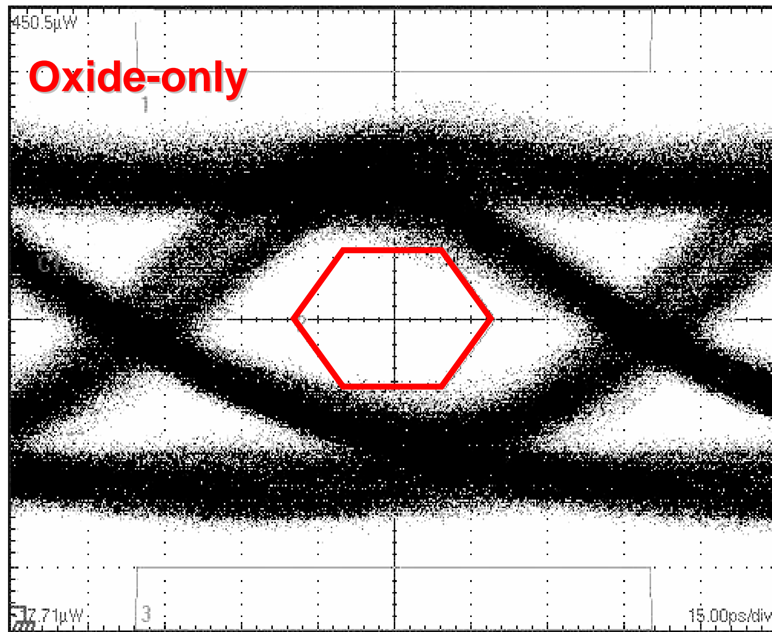

(a) Oxide-only VCSEL

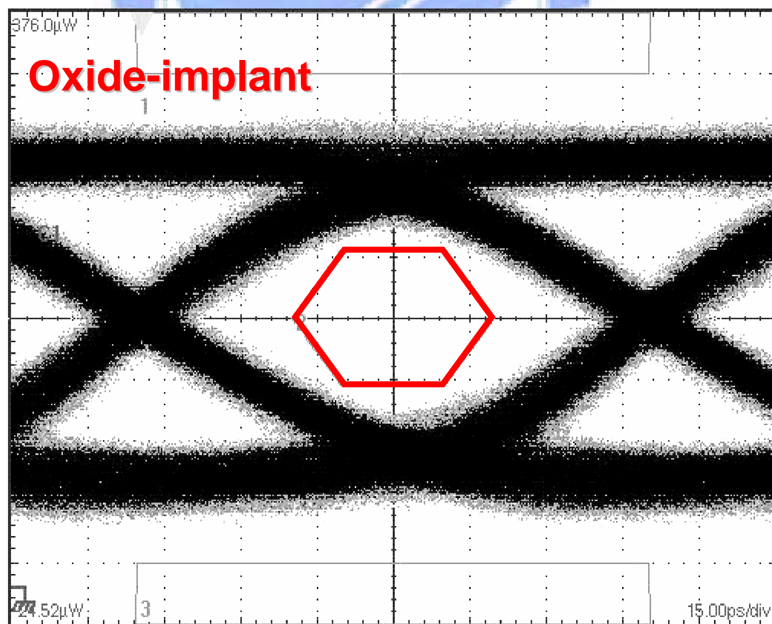

(b) Oxide-implant VCSEL

Figure 4-5 Eye-diagram for oxide-only and oxide-implant VCSELs

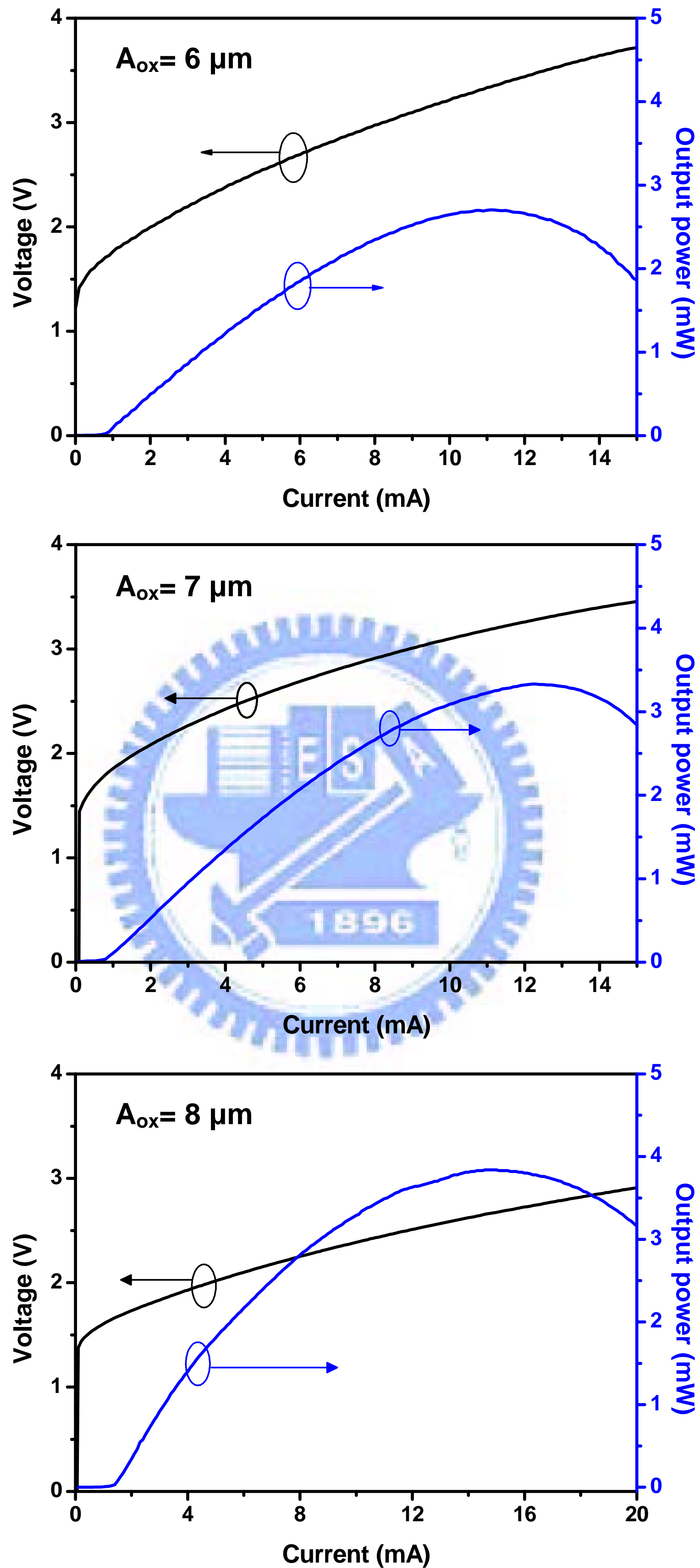

Figure 4-6 Typical LIV curve for VCSELs with different oxide aperture size as 6, 7, and 8 μm

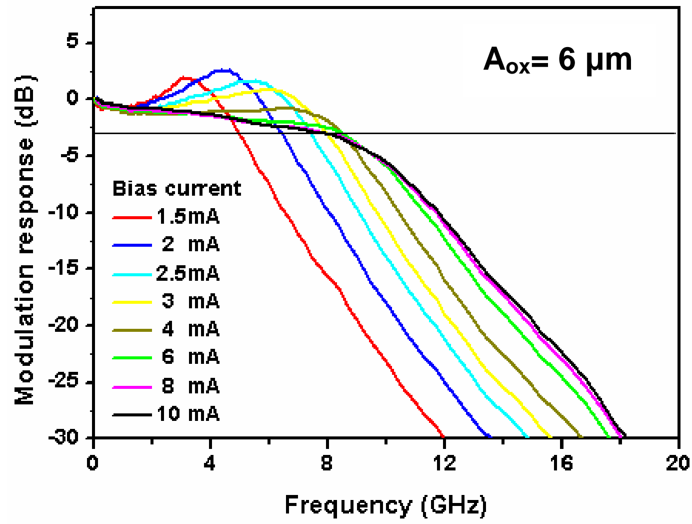

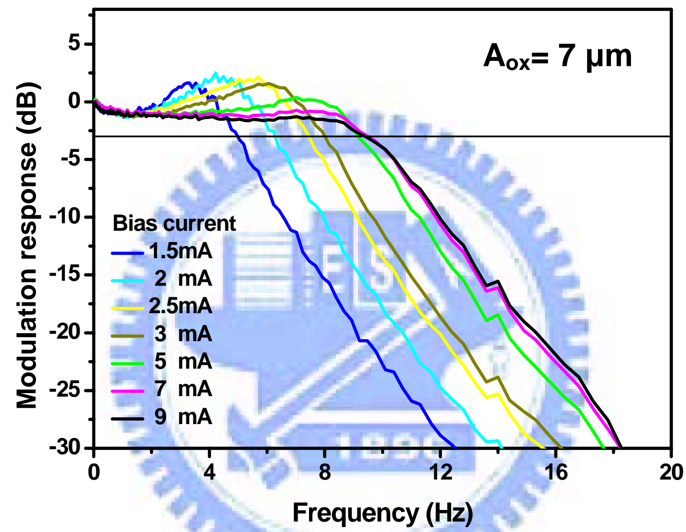

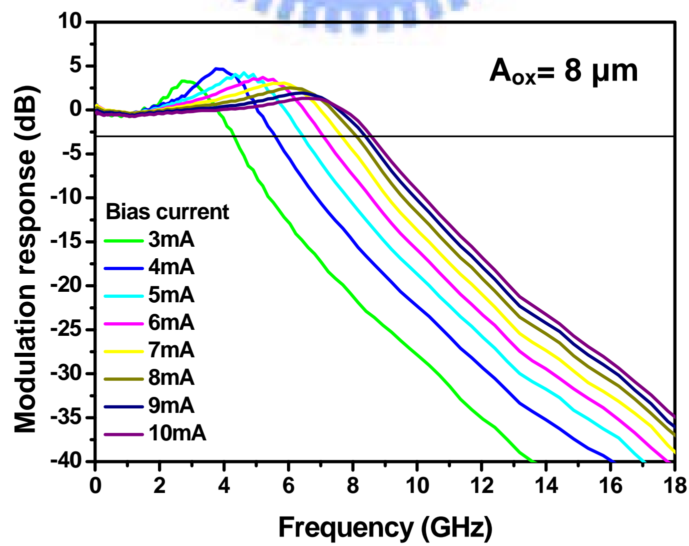

Figure 4-7 Modulation response of VCSELs with difference oxide aperture as 6, 7, and 8 μm

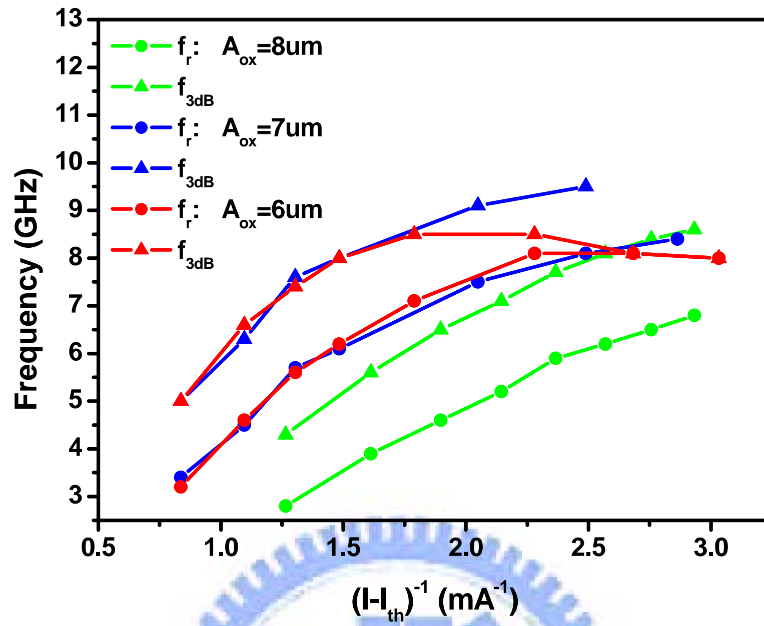

Figure 4-8 Resonance and 3dB frequency as a function of $(I-I_{th})^{1/2}$ for difference oxide aperture VCSELs

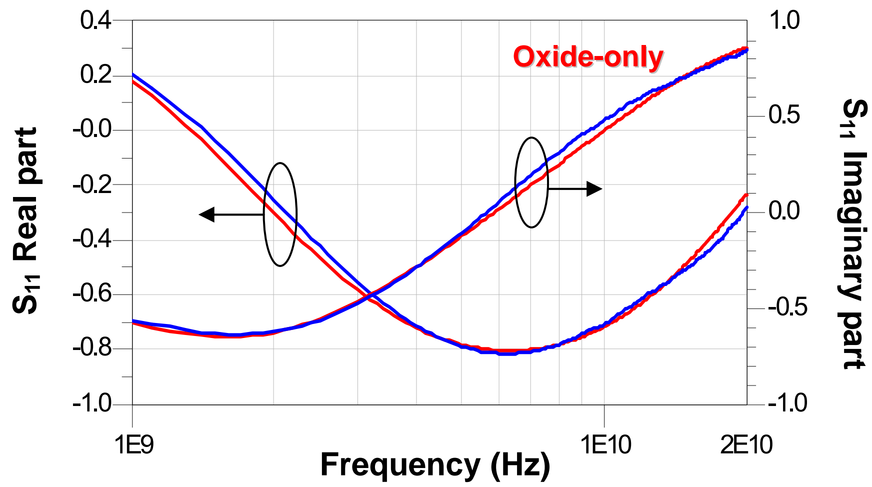

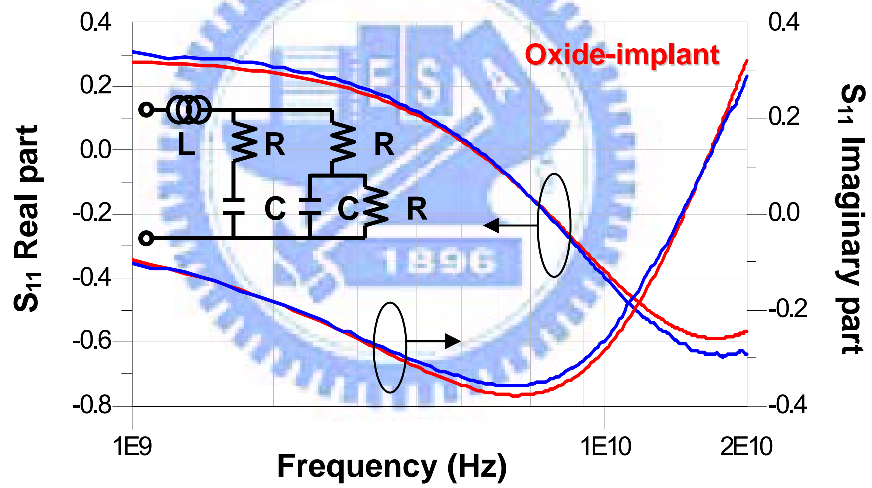

Figure 4-9 Real and imaginary S11 parameter versus frequency from model and measured data (blue line is measured data, red line is simulated data)

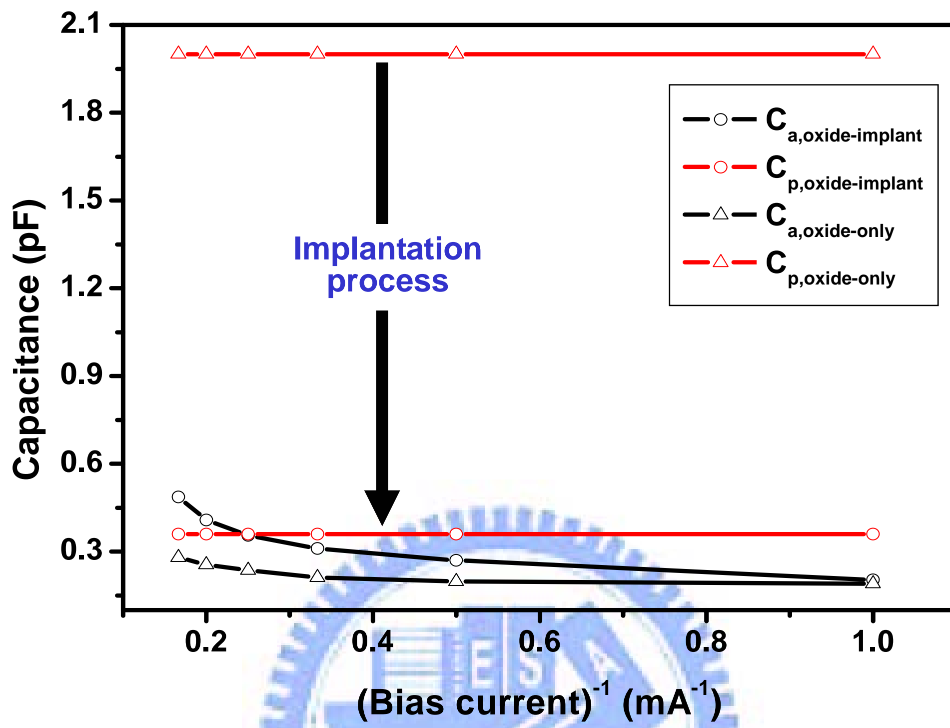

Figure 4-10 Compared capacitances of oxide-only and oxide-implant VCSELs

Oxide-only						
	L (nH)	Ca (pF)	Cp (pF)	Ra (Ω)	Rm (Ω)	Rp (Ω)
1mA	0.331	0.190	2	230	52	4.9
2mA	0.331	0.198	2	108	52	4.9
3mA	0.331	0.211	2	72	52	4.9
4mA	0.331	0.236	2	57	52	4.9
5mA	0.331	0.255	2	45	52	4.9
6mA	0.331	0.280	2	45	52	4.9

Table 4-1 Equivalent circuit elements at different bias current for oxide-only VCSEL

Oxide-implant						
	L (nH)	Ca (pF)	Cp (pF)	Ra (Ω)	Rm (Ω)	Rp (Ω)
1mA	0.229	0.203	0.359	89	58	8.9
2mA	0.229	0.270	0.359	42	58	8.9
3mA	0.229	0.310	0.359	33	58	8.9
4mA	0.229	0.355	0.359	28	58	8.9
5mA	0.229	0.408	0.359	24	58	8.9
6mA	0.229	0.486	0.359	14	58	8.9

Table 4-2 Equivalent circuit elements at different bias current for oxide-implant VCSEL

Chapter 5

Conclusion

We have performed experimental study of small signal modulation behavior of 850nm oxide-only and oxide-implant VCSELs. The simple planar VCSEL structure is fabricated with difference oxide aperture diameters.

We have found that implantation process gives VCSEL with excellent high speed performance without semi-isolating substrate. Modulation bandwidth of oxide-only VCSEL is limited caused to parasitic capacitance demonstrated by equivalent circuit modeling. The equivalent circuit model is established benefit for modifying VCSEL structure epitaxy and process. Otherwise, we search the best oxide aperture size of oxide-implant VCSEL for high speed operation as 7 μm.

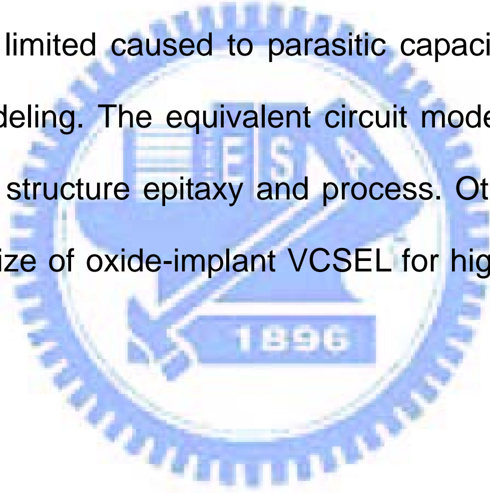

Reference

[1] H. Soda, K. Iga, C. Kitahara, and Y. Suematsu, “GaInAsP/InP surface emitting injection lasers,” Japanese Journal of Applied Physics, vol.18, pp.2329-2330, 1979.

[2] K. Iga, F. Koyama, and S. Kinoshita, “Surface-emitting semiconductor lasers,” IEEE Journal of Quantum Electronics, vol.24, pp.1845-1855, September 1988.

[3] H. E. Li, and K. Iga, “Vertical cavity surface emitting laser,” Springer, Berlin, New York, 2003.

[4] T. Honda, T. Shirasawa, N. Mochida, A. Inoue, A. Matsutani, T. Sakaguchi, F. Koyama, and K. Iga, "Design and fabrication processes consideration of GaN-based surface emitting lasers," Trans. IEICE, J81-C-II, pp.97-104, 1998.

[5] “2003 年光電半導體產業及技術動態調查報告,” PIDA, 2004.

[6] R. Brand, “10 gigabit Ethernet interconnection with wide area networks,” 10GEA, March 2003

[7] K. L. Lear, A. Mar, K. D. Choquette, S. P. Kilcoyne, R. P. Schneider jr., and K. M. Geib, “High-frequency modulation of oxide-confined vertical cavity surface emitting lasers,” Electron. Letter, pp.457-458, February 1996.

[8] C. Carlsson, H. Martinsson, R. Schatz, J. Halonen, and A Larsson, “Analog modulation properties of oxide confined VCSELs at microwave frequencies,” IEEE Journal of Lightwave Technology, vol.20, pp.1740-1749, September 2002.

[9] C. H. Chang, L. Chrostowski, and J. Chang-Hasnain, “Parasitics and design considerations on oxide-implant VCSELs,” IEEE Photonics Technology

Letters, vol.13, December 2001.

[10] A. K. Dutta Dutta, H. Kosaka, K. Kurihara, Y. Sugimasa, and K. Kasahara, "High-speed VCSEL of modulation bandwidth over 7.0 GHz and its application to 100 m PCF datalink," IEEE Journal of Lightwave Technology, vol.16, pp.870-8755, May 1998.

[11] A. Larsson, C. Carlsson, J. Halonen, and R. Schatz, “Microwave modulation characteristics of 840nm oxide confined / proton implanted VCSELs,” Microwave Photonics technical report, October 2001.

[12] A. Larsson, C. Carlsson, A. Haglund, J. Halonen, and R. Schatz, “Microwave modulation characteristics of BCB-planarized oxide confined 850nm VCSELs,” Microwave Photonics technical report, June 2002.

[13] A. N. AL-Omari, and K. L. Lear, “Polyimide-planarized vertical cavity surface emitting lasers with 17.0GHz bandwidth,” IEEE Photonics Technology Letter, vol.16, pp.969-971, April 2004.